REPORT DOCUMENTATION PAGE

Form approved
OMB No. 0704-0188

1. AGENCY USE ONLY *(Leave blank)*	2. REPORT DATE	3. REPORT TYPE AND DATES COVERED
	31 July 1996	Final Technical Report, 940901 - 951231

4. TITLE AND SUBTITLE
NANODESIGNING OF MULTIFUNCTIONAL CERAMICS

5. FUNDING NUMBERS
AFOSR F49620-93-1-0259

6. AUTHOR(S)
ILHAN A. AKSAY

AFOSR-TR-96

0469

7. PERFORMING ORGANIZATION NAMES(S) AND ADDRESS(ES)
Department of Chemical Engineering and Princeton Materials Institute
Princeton University
Princeton, NJ 08544

9. SPONSORING/MONITORING AGENCY NAME(S) AND ADDRESS(ES)
Air Force Office of Scientific Research, Chemistry and Materials Sciences
110 Duncan Ave., Suite B115, Bolling AFB
Washington DC 20332-0001

NA

10. SPONSORING/MONITORING AGENCY REPORT NUMBER
93-1-0259

11. SUPPLEMENTARY NOTES
The views, opinions, and/or findings contained in this report are those of the author(s) and should not be construed as an official Department of the Air Force position, policy, or decision, unless so designated by other documentation.

12a. DISTRIBUTION/AVAILABILITY STATEMENT
Approved for public release; distribution unlimited.

12b. DISTRIBUTION CODE

13. ABSTRACT *(Maximum 200 words)*

The work presented in this report details the activities of the Ceramic Materials Laboratory at Princeton University during the period 1992 through 1995. The goals of the project were to develop methods for processing ceramic composites at the nanometer scale using a variety of processing methodologies. Materials systems included high (>1000°C) and low (<1000°C) materials (ceramic/ceramic and ceramic/metal composites respectively) and multifunctional ceramics. Several different approaches were used for the nanodesigning of materials: (i) reaction sintering, (ii) exsolution, and (iii) coassembly; two classes of materials were used as model systems for these processing methods: (i) structural ceramics and (ii) functional ceramics. Shape forming research emphasized field assisted patterning, gel-casting, osmotic consolidation, and coassembly. Modeling efforts continued on (i) the interaction between inorganic materials and organic surfactants in the coassembly of particles an mesoporous matrices and (ii) the sintering of nanosized particles. In general, our studies demonstrated that nanometer scale inclusions in oxide and non-oxide ceramic matrices can be achieved by any one of several different routes. Different materials systems require different methods of processing in order to achieve the level of control desired for the manufacture of nanocomposites.

14. SUBJECT TERMS
ceramics, multifunctional, hierarchical design, nanometer scale

15. NUMBER OF PAGES
39

16. PRICE CODE

17. SECURITY CLASSIFICATION OF REPORT	18. SECURITY CLASSIFICATION OF THIS PAGE	19. SECURITY CLASSIFICATION OF ABSTRACT	20. LIMITATION OF ABSTRACT
UNCLASSIFIED	UNCLASSIFIED	UNCLASSIFIED	UNLIMITED

Nanodesigning of Hierarchical Multifunctional Ceramics

Air Force Office of Scientific Research
Final Technical Report for Grant No. F49620-93-1-0259

I. A. Aksay, **Principal Investigator**

September 1, 1992 through December 31, 1995

Department of Chemical Engineering and
Princeton Materials Institute
Princeton University
Princeton, New Jersey 08544-5263

Table of Contents

Table of Contents ii
List of Figures iv
Executive Summary 1
Technical Report 3
1. Applications 3
1.1. Processing Methods 3
1.1.1. Pressure Filtration of Seeded Boehmite Gels for Monolithic α-Alumina 4
1.1.2. The Osmotic Consolidation of Ceramic Suspensions 4
1.1.3. Field-Induced Pattern Formation in Colloidal Dispersions 5
1.1.4. Field-Induced 2-Dimensional Nanolaminates 7
1.2. Mullite Matrix Composites (Ceramic/Ceramic Composites) 8
1.2.1. Effect of Cr_2O_3 and MnO_2 Additives on the Mechanical Properties of Colloidally Processed Alumina 8
1.2.2. Processing of Nanocomposites Silicon Nitride-Mullite-Alumina By Reaction Sintering 9
1.2.3. Processing of a Mullite Matrix, Molybdenum Disilicide Reinforced Composite 10
1.2.4. Processing of Nanocomposite Powders 10
1.3. Ceramic/Metal Composites (<1000°C) 11
1.3.1. Processing of SiC/Al-Si Alloy Laminated and Monolithic Composites 11
1.3.2. The Wetting Behavior of SiC with Al(Si) Alloys 12
1.4. Methods for Obtaining High Temperature (>1000°C) Ceramic/Metal Composites 12
2. Functional Ceramics 14
2.1. Formation of $BaTiO_3$ Particles by Low Temperature (<100°C) Hydrothermal Processing 14
2.2. Theory of the Size Effect of Small $BaTiO_3$ Particles 16
2.3. Low Temperature (<500°C) Processing of PZT Thin Films Through Seeding 17
2.4. Piezoelectrical Properties of $Pb(Zr_{0.52}Ti_{0.48})O_3$ Sintered at Low Temperature 18
2.5. Pressure Filtration of Hydrothermal $BaTiO_3$ Powder 19
2.6. Low Temperature Processing of $BaTiO_3$ Thin Films 19
3. Model Systems 20
3.1. Formation and Sintering in Nanometer Size Particles 20
3.1.1. Surfactant Mediated Deformation of Gold Agglomerates 20
3.1.2. Neck Formation of Nanometer Sized Particles 22
3.2. Mesoporous Silicate and Aluminosilicate Materials 23
3.2.1. Self Assembling Mesoscopic Materials 24
3.2.2. Thin Film Formation of Mesoporous Silicate 24
3.2.3. Fabrication and Characterization of Mesosilicate Nanocomposites 26
3.3. The Formation of Ceramic/Cellulose Cellular Composites 26
4. Personnel 33
5. Manuscripts 34
5.1. Published Journal Articles 34

5.2. Chapters in Books and Proceedings 34
5.3. Patents and Invention Disclosures 36
6. Biographical Sketches 37
6.1. Ilhan A. Aksay 37
6.2. Daniel M. Dabbs 37
6.3. David L. Milius 38
6.4. Wan Y. Shih 38

List of Figures

Fig. 1: Processing methods for the production of nanocomposites. 3
Fig. 2: Sintered densities of seeded (•) and unseeded boehmite (□). 4
Fig. 3: A schematic diagram of our model system: a spherical, particle-containing bolus (region 1) nested inside clear ambient fluid (region 2)....5
Fig. 4: Two examples of the deformation of a colloidal dispersion via an applied electric field. Panels (a)-(d) and (e)-(h) are video sequences taken after a steady DC field was applied to a spherical cloud of a $BaTiO_3$ dispersion nested inside clear castor oil. The dispersion consisted of 100 nm $BaTiO_3$ particles in castor oil (0.025% by volume). The resulting images have been colored to enhance the contrast between particle containing regions and clear fluid. In the two experiments the conductivity mismatch between the inner and outer bolus region was reversed by dissolving a trace amount of tetrabutylammonium tetraphenylborate (0.2×10^{-3} mol·dm^{-3}) either in the inner region, sequence (a)-(d), or in the surrounding clear fluid, sequence (e)-(f). In both cases the magnitude of the applied field was 2000 Vcm^{-1}, applied in the vertical direction. 6
Fig. 5: Streamline pattern for flow engendered by a circular shaped cloud of a dispersion immersed in a clear fluid with a lower conductivity and dielectric constant. 7
Fig. 6: Monolayer of colloidal polystyrene particles formed by EPD. 8
Fig. 7: HREM image of $BaTiO_3$ particles formed within one minute of mixing the precursors. The nuclei precipitate to form an aggregate of crystallites with matching crystal lattices. 15
Fig. 8: The change in the ferroelectric transition temperature T_c as a function of particle size. 17
Fig. 9: Because of the size dependence of T_c at a given temperature, the dielectric constant ε peaks at a certain size L of the particles....17
Fig. 10: (a) Ramified gold agglomerate with twin domains (domain size<10nm). (b) Final gold particles (~24nm average diameter). 21
Fig. 11: ATR spectra for (i) sodium citrate in aqueous solution and (ii) gold particles stabilized by citrate ions in aqueous suspension. 22
Fig. 12: Smooth metal surface with constant potential (top) and surface containing cusp of low potential (bottom). The high density of adsorbates within the cusp forces migration of metal atoms from the apex, sharpening the cusp and eventually leading to separation....22
Fig. 13: Necking between nanometer sized particles....23
Fig. 14: TEM images of (a) the lamellar morphology, (b) the cubic phase with Ia3d symmetry viewed along its [111] zone axis, and (c) the hexagonal phase viewed along its [001] zone axis (bars = 30 nm). 24
Fig. 15: XRD patterns from a time-resolved experiment. The numbers with the peak labels are the square of the peak indices. (a) 20min exposure taken during the first 20 min of heating. (b) 20min exposure taken after 160 min of heating. The two peaks are consistent with a lamellar structure, as shown by the peak labels. (c) The average of six 20min exposures taken after 20 h of heating. The 8 peaks are consistent with

Ia3d symmetry, as shown by the peak labels. There were two faint rings at higher q which did not match the Ia3d pattern and are not explained. 25
Fig. 16: SEM micrographs of infiltrated wood (a) before pyrolysis and (b) after pyrolysis at 600°C. The wood's cellular structure has been replaced by silica in (b). 27

NANODESIGNING OF HIERARCHICAL MULTIFUNCTIONAL CERAMICS

Ilhan A. Aksay

Executive Summary

This report is the final technical report for AFOSR grant number F49620-93-0259, covering the period September 1, 1992, through December 31, 1995. This is the final segment of the project entitled "Nanodesigning of Hierarchical Multifunctional Ceramics" that began October 1, 1990 at the University of Washington, Seattle, which extended the preceding project sponsored by the AFOSR "Microdesigning of Lightweight/High Strength Ceramic Materials" from 1983 through 1990 (Grant Nos. AFOSR-83-0375, 1 October 1983 to 30 November 1986, and AFOSR-87-0114, 1 December 1986 to 28 February 1991). On September 1, 1992, the project that is the subject of this report was transferred from the University of Washington to Princeton University.

The principal focus of our earlier projects under AFOSR sponsorship from 1983 to 1991 was to establish guidelines for processing low density (< 3.0 g/cc) and high strength (> 800 MPa) ceramic matrix composite materials for structural applications. The achievements of the first six years of the research program have led to the development of improved ceramic fabrication processes involving the use of colloidal dispersion and consolidation methods. Although significant gains in understanding the processing of dense ceramic matrix composites resulted from that work, it became apparent that our understanding of the structural and optoelectronic properties of composite materials failed as we approached length scales between 1 to 100 nm. Within this size range our knowledge of materials synthesis and processing by deliberate design is the weakest, yet we came to understand that nanometer-scale interactions strongly determine the macroscopic properties of materials. In response, our work over the preceding past four years shifted to those address issues related to the *nanodesigning* of ceramic matrix composites using colloidal dispersions and molecular precursors.

The overall goal of our work has been to demonstrate the practical advantages of applying the concept of hierarchy to developing superior macroscopic properties in ceramic matrix materials. To this end, we seek to design materials with predictable properties, requiring that structural development be closely controlled at each step during processing, beginning with mixing (at the nanometer scale) and continuing through the densification of the constituent phases (at the micron and larger scales). For example, ceramic/ceramic nanocomposites have been reported to have significantly improved mechanical properties (§1.2) yet it is also claimed that these observations are merely the result of poor sample preparation. We have developed reproducible methods for synthesizing nanocomposite powders to be used to fabricate test specimens for mechanical testing. A model describing the effect of nanometer-sized inclusions in a continuous matrix has been proposed.

The research projects summarized in the following sections were all selected to meet the goal of designing multifunctional ceramics for structural and functional applications with a starting point at the atomic and nanometer level, recognizing that modeling of physical phenomena is a requisite part of any integrated materials research group. A colloidal approach to processing has been taken in the most part, stemming from our recognition that this will be the most feasible approach for the production of large scale devices and components. Tasks within

the program are categorized into three areas: (i) applications (§1.), (ii) functional ceramics (§2.), and (iii) model systems (§3.). In the first task area the research projects are concerned primarily with the fabrication of monoliths, built up from nanoscale structures. In the second task area the key emphasis is on the application of fundamental concepts generated in our previous projects to produce novel composites that can be utilized in novel optoelectronic applications. Finally, model experiments are designed to (i) provide guiding principles for applications and functional ceramics and (ii) develop new concepts in materials processing.

Manuscripts and theses that have been completed within the reporting period are included in the Appendices.

Technical Report

1. Applications

In this portion of our project the emphasis is on basic issues in the processing of hierarchical materials. We choose to work at the nanometer scale as this holds the most promise for fabricating multifunctional materials with the desired properties. Proper fabrication of applied materials involves controlling each step of manufacture, from the synthesis of the starting materials to the production of the final monolith, making this area the most wide-ranging of the three task areas described above. Grouped within the study of applications are task areas on (i) processing methods (§1.1), (ii) ceramic/ceramic composites (§1.2), and (iii) low and high temperature ceramic/metal composites (§§1.3, 1.4).

1.1. Processing Methods

Investigators: ***Matt Trau, Fatih Dogan, John Mellowes, James S. Vartuli, Dudley A. Saville, and Ilhan A. Aksay***

Processing methods for the production of nanocomposites are shown schematically in Fig. 1. Of the seven methods shown in the diagram, we avoid milling due to the lack of process control. Generally, we seek to develop methods that will allow the controlled fabrication of hierarchical nanocomposites through chemical techniques, physical manipulations, or a combination of the two. Ultimately, the success of any proposed process method is the production of materials which exhibit the desired mechanical and/or optoelectronic properties. In all of the methods described below, we seek to produce samples for testing under realistic conditions. To achieve this, we first must focus on developing suitable methods for producing the desired materials.

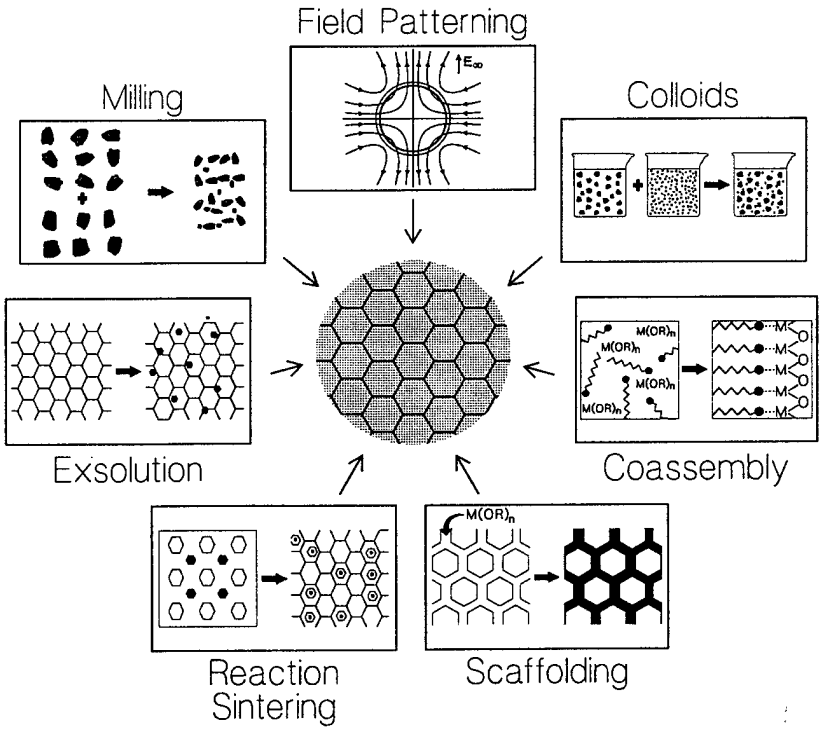

Fig. 1: Processing methods for the production of nanocomposites.

1.1.1. Pressure Filtration of Seeded Boehmite Gels for Monolithic α-Alumina

Previous research has shown that fully dense α-alumina of millimeter dimensions can be processed by sintering seeded boehmite gels in the temperature range of 1300 to 1400°C.[1-8] However, the processing of larger size samples has been hindered due to excessive cracking of the gels during drying. We have shown that this problem can be eliminated by densifying the gels by pressure filtration prior to drying. Acid stabilized suspensions of boehmite seeded with α-alumina have been gelled and pressure filtered to green densities of ~58%. Samples as large as 2.5 cm in diameter were sintered to densities higher than 99.4% TD at 1300°C without any cracking.

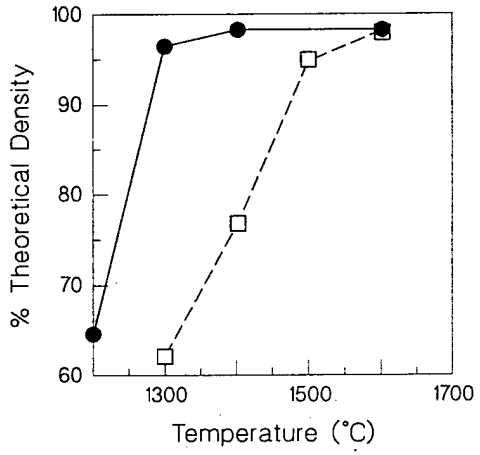

Fig. 2: Sintered densities of seeded (●) and unseeded boehmite (□).

Seeded samples can be sintered crack-free and without deformation. The sintering densities of seeded samples were 99.4 and 99.7% of the theoretical density at 1300 and 1400°C, respectively; whereas, unseeded samples could be sintered to 98% of the TD only at temperatures above 1600°C (Fig. 2). A homogeneous microstructure with an average grain size of 2 μm was obtained with the seeded samples. This work demonstrates the importance of seeding as a processing tool in fabricating high density ceramics. These results are now being applied to functional ceramics such as PZT thin films (§2.3) and mesoporous silicates (§3.2.2).

1.1.2. The Osmotic Consolidation of Ceramic Suspensions

The fabrication of ceramic monoliths with consistent mechanical properties requires the production of highly dense and uniform green bodies. As the particle size decreases to the nanometer scale the effective packing density is found to decrease due to the increased attraction between the fine particles; aggregation is uncontrolled, highly porous ramified structures form, and the green density declines.[9] Model studies within this research project have used ultrafine gold particle suspensions to examine the sintering of nanoscale materials from colloidal suspensions (see §3.1.2). Other studies performed within our research group but not supported in the AFOSR program have studied the compaction behavior of powder suspensions with the goal of approaching slip-cast green densities. Miller and Zukoski have demonstrated a method by which extremely high pressures (~12MPa) can be exerted on suspensions and gels using osmotic pressure.[10] They report volume densities in excess of 60 vol% for alumina green bodies by this method. For the proposes of our project, osmotic consolidation offers a method by which consistently high green densities can be achieved in suspensions of ultrafine particles.

Miller and Zukoski obtained very dense alumina green bodies by placing dilute alumina suspensions (20 volume percent) inside dialysis bags immersed in a concentrated poly(ethylene oxide) (PEO) solution. Our modification of this procedure sought to maximize the amount of material that could be processed and to minimize the time necessary to achieve high densities. To meet these two goals, our procedure uses a constant flow of PEO through a ~2m long dialysis tube (2.1cm diameter) immersed in a ceramic suspension (initially 1 vol% AKP-30 alumina). The PEO solution could be recycled simply by removing the excess water by heating. Using this

method, the initial water extraction rate was measured to be ~350mL/h; the final water extraction rate was found to be 50mL/h. Green densities as high as 58% have been achieved.

Difficulties with the process include: (i) maintaining pH balance between the suspension and the PEO solution (differences significantly reduce the effective osmotic pressure); (ii) the increasing viscosity of the suspension as density increases; and (iii) the formation of nearly impermeable cake layer at the membrane. These issues are the current and future task areas for developing a useful application of osmotic pressure consolidation for use with ceramic suspensions.

1.1.3. Field-Induced Pattern Formation in Colloidal Dispersions

The formation of patterned colloidal structures has many applications in materials processing. Examples include catalytic support honeycombs produced by extrusion,[11,12] hierarchical electronic devices made with ceramic multilayers,[13] electro-rheological fluids,[13-16] and "smart materials" formed from patterned composites.[17] Moreover, nested levels of structural hierarchy in composite materials can impart vastly superior properties over a homogeneously structured material.[18-21] Due to the intrinsic dimensional limitations of mechanical forming, pattern formation in such materials has hitherto been restricted to length scales larger than a few tens of microns. We have been investigating the use of electrohydrodynamic forces which act directly on non-homogeneous regions in a colloidal dispersion so as to form patterned colloidal dispersions. Once the patterns are formed, the structures can be set by solidifying the fluid matrix via gelation or polymerization.

To illustrate the process, we used 100 nm barium titanate ($BaTiO_3$) particles prepared via a hydrothermal process (see §2.1) and dispersed in castor oil. Barium titanate was chosen because it has an extremely high dielectric constant (between 300 and 10,000, depending on its crystalline form), and is a technologically useful material in both the electronic and optical component industries. Castor oil was chosen as the fluid medium because: (i) it has a low conductivity ($\sigma = 1.8 \times 10^{-11}$ Sm^{-1}); (ii) fatty-acid based oils are good dispersing media for barium titanate particles; (iii) its conductivity may easily be varied over a wide range by doping with small amounts of soluble organic salts (e.g., tetrabutylammonium tetraphenylborate, TBATPB); and (iv) its viscosity is similar to those of polymerizable silicone oils used to prepare colloidal barium titanate structures within a solid silicone polymer matrix. To form the system depicted in Fig. 3, a dilute dispersion of barium titanate particles (0.025 vol%) in castor oil was injected into clear castor oil fluid via a pin hole in a metal electrode. Slow injection of the dispersion into the clear fluid results in a spherical bolus of the dispersion nested within clear castor oil [cf. Figs. 4(a) and (e)]. The 4 × 4 cm metal electrodes were 1.5 cm apart; the diameter of the colloidal bolus was approximately 5 mm.

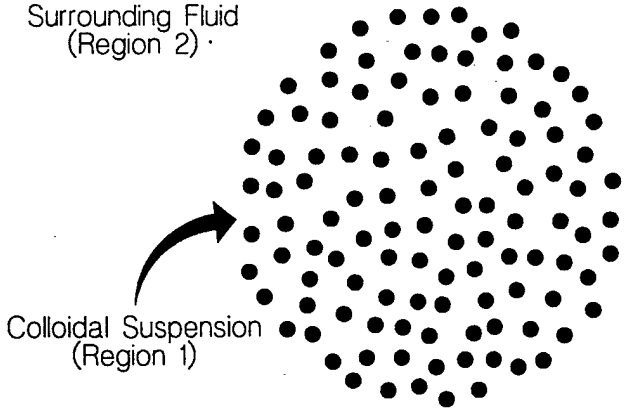

Fig. 3: A schematic diagram of our model system: a spherical, particle-containing bolus (region 1) nested inside clear ambient fluid (region 2).

Fig. 4 illustrates the results for two experiments, the first in which the conductivity of the dispersion is higher than that of the

surrounding fluid and the second in which this was reversed. The series of images show the effect of applying a 2000 Vcm^{-1} electric field over a time interval of approximately 0.2 seconds. In sequence (a)-(d) (higher conductivity in the dispersion), the spherical droplet deforms immediately in the direction of the applied field and continues to stretch until it collides with the top electrode to form a near-perfect column. The column remains intact for several seconds. In the (e) to (h) sequence (higher conductivity in the surrounding fluid), a different flow pattern is caused by application of the field. The spherical bolus deforms orthogonal to the applied field,

Fig. 4: Two examples of the deformation of a colloidal dispersion via an applied electric field. Panels (a)-(d) and (e)-(h) are video sequences taken after a steady DC field was applied to a spherical cloud of a $BaTiO_3$ dispersion nested inside clear castor oil. The dispersion consisted of 100 nm $BaTiO_3$ particles in castor oil (0.025% by volume). The resulting images have been colored to enhance the contrast between particle containing regions and clear fluid. In the two experiments the conductivity mismatch between the inner and outer bolus region was reversed by dissolving a trace amount of tetrabutylammonium tetraphenylborate (0.2×10^{-3} $mol \cdot dm^{-3}$) either in the inner region, sequence (a)-(d), or in the surrounding clear fluid, sequence (e)-(f). In both cases the magnitude of the applied field was 2000 Vcm^{-1}, applied in the vertical direction.

forming a disk shape which continues to expand laterally. After some time, a film forms across the bottom electrode. Steady (DC) fields were used to generate all of the patterns shown in Fig. 4 but the direction and speed of the motion was found to be insensitive to the field's polarity. Similar flow patterns are induced by applying low frequency AC fields (approximately 100 Hz) which shows that the particle motions are not the result of electrokinetic phenomena but can be explained in terms of an electrohydrodynamic flow.

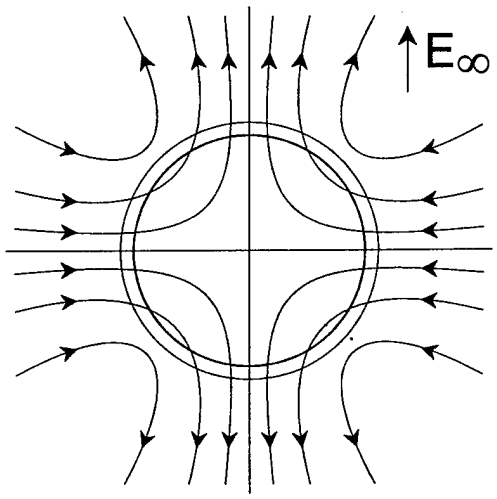

Fig. 5: Streamline pattern for flow engendered by a circular shaped cloud of a dispersion immersed in a clear fluid with a lower conductivity and dielectric constant.

A qualitative picture of the flow patterns can be obtained from a simple model where the dielectric constant and conductivity distributions are prescribed. This was done for situations where a transverse electric field acts on a circular region with dielectric constant ε_1 and conductivity σ_1, surrounded by a region with properties σ_2 and ε_2 and each property varies smoothly in the (thin) transition zone. Fig. 5 depicts the situation and shows the streamlines of the velocity field calculated when the dielectric constant and conductivity of the interior exceed those in the exterior. In this case the dispersion would be drawn out into a ribbon-like shape oriented parallel to the field (in three dimensions the shape would be a cylinder). The flow direction reverses when the conductivity of the interior is less than that of the exterior and the sample takes up a flat configuration orthogonal to the field. These qualitative features are in complete agreement with our experimental observations.

Although the experiments presented here have been performed solely on $BaTiO_3$/castor oil dispersions, this technique is in no way restricted to this system. Indeed, provided that there exists a sufficient mismatch in conductivity and/or dielectric constant, any colloidal dispersion nested within any ambient fluid may be manipulated in a similar manner (§1.1.4).

1.1.4. Field-Induced 2-Dimensional Nanolaminates

We have been conducting experiments to determine whether colloidal nanolaminates of controlled morphology can be produced by the technique of electrophoretic deposition (EPD).[22,23] EPD of colloidal particles is a long established technique for the production of macroscopic particulate films, however, hitherto has not been successfully applied to the formation of mono- or multilayered colloidal films with precise morphological control.[23] To observe the deposition mechanism in microscopic detail, we have constructed an apparatus consisting of an optically transparent indium tin oxide (ITO) electrode coupled to an optical microscope. A video camera is used to record the dynamics of the particles depositing on the electrode under the influence of an applied electric field.

Initial experiments have been performed on silica (900nm diameter) and polystyrene (2-4μm diameter) particles. These experiments have revealed very surprising results: Provided the colloidal stability of the particles is maintained with respect to each other and with respect to the electrode and in the presence of a sufficiently strong applied electric field, colloidal particles are attracted to each other on the surface of the electrode. This (lateral) attraction force acts in a

direction normal to the applied field and is strong enough to bring the particles together to form ordered structures, such as 2-dimensional colloidal crystals (Fig. 6). This observed attraction is surprising given that a strong repulsion would be expected from electrostatic considerations: all of these particles are similarly charged and contain a diffuse ionic cloud (double layer) which will be polarized in the presence of the field; as these particles approach each other on the surface of the electrode, electrostatic repulsion should be experienced both from monopole and dipole interactions. Currently, we believe that the observed attraction is a result of a combination of the electrochemical reaction at the electrode interface (which allows for current to pass through the system) and fluid flow which is set in motion as a result of this reaction.

Fig. 6: Monolayer of colloidal polystyrene particles formed by EPD.

It has been observed that the magnitude of the lateral attraction between the particles can be modulated by either the amplitude or frequency of the applied external field. The ability to modulate the strength of the lateral attraction allows the formation of different colloidal phases on the surface of the electrode (e.g., crystalline, liquid and gaseous); phase transitions can be conveniently induced by varying the amplitude of the applied field. By cycling between liquid and solid phases (cyclic annealing), particles in the electrophoretically deposited layer can be continually redistributed until a perfect colloidal monolayer is formed (i.e., all EPD particles are located in the first layer, with no particles populating the second or third layers). Once the monolayer is formed, it can be "frozen" into place by inducing coagulation via the applied field. Using this approach, submicron monolayers of silica and polystyrene particles have been assembled and "frozen". We expect that this technique can be generally applied to any type of colloidal particles (§1.1.3). Research on the formation of controlled multilayered structures is continuing.

1.2. Mullite Matrix Composites (Ceramic/Ceramic Composites)

Investigators: Richard A. Brynsvold, David L. Milius, Fatih Dogan, Yoshihiro Sakka, Dilshad Shahid, Daniel M. Dabbs, and Ilhan A. Aksay

1.2.1. Effect of Cr_2O_3 and MnO_2 Additives on the Mechanical Properties of Colloidally Processed Alumina

MnO_2 and Cr_2O_3 are known to increase the hardness of alumina ceramics.[24] The effect of these additives on the microstructural evolution and mechanical properties of α-alumina is part of our continuing work on the processing of ceramic matrix composites. In order to achieve a uniform distribution of the additives, we coated submicron size alumina particles with soluble chromium- and manganese acetates. Suspensions were freeze dried to process granules which were then used in the preparation of compacts by dry pressing and slip casting. Chromia, as a solid solution additive, inhibited the grain growth. Excessive grain growth was observed with

MnO_2 additions. In both cases, an increase in hardness was observed. Tensile strength increased with Cr_2O_3 and decreased with MnO_2 doping. The results were correlated with the microstructural features.

The hardness of alumina increased with both additives. Slip cast samples with Cr_2O_3 and MnO_2 additives yielded microhardnesses up to ~2600 and 2700, respectively. These values are higher than the hardnesses reported in previous studies.[24] We attribute these higher values to the homogeneity of the slip cast samples. Although we have not yet confirmed the respective mechanisms, additive, precipitation hardening is expected in the case of MnO_2 whereas in the case of Cr_2O_3 solid solution hardening is thought to be the dominant mechanism.

In the case of tensile strength, however, MnO_2 containing samples were lower in strength whereas the strength of Cr_2O_3 containing samples increased from 500 to 700 MPa. We attributed the decrease in the first case to significantly larger size (100 μm) grains since these grains can act as critical flaws. However, since in the case of chromia addition the grain size does not change noticeably in comparison that of the undoped samples, we attributed the increase in this case to the solid solution effect of the chromia. Studies are underway to confirm these suspected mechanisms.

1.2.2. Processing of Nanocomposites Silicon Nitride-Mullite-Alumina By Reaction Sintering

In the first phase of this work we developed a new method for processing SiC-mullite-Al_2O_3 nanocomposites by the reaction sintering of green compacts prepared by colloidal consolidation of a mixture of SiC and Al_2O_3 powders.[25] The surface of the SiC particles was first oxidized to produce silicon oxide and to reduce the core of the SiC particles to nanometer size. Next, the surface of silicon oxide was reacted with alumina to produce mullite. This process results in particles with two kinds of morphologies: nanometer-sized SiC particles that are distributed in the mullite phase and mullite whiskers in the SiC phase. Both particle types are immersed in an Al_2O_3 matrix.

Densities greater than 95% of theoretical were obtained by sintering fine SiC and alumina at 1600°C for two hours in argon atmosphere. This process offers several advantages and thereby warrants further research: (i) it eliminates the need to reduce the particle size of the inclusion phase to the nanometer range by milling and thus provides better control in minimizing impurities; (ii) due to a volume increase during reaction sintering, sintering shrinkages are lower; and (iii) the presence of amorphous silica as a transient phase results in enhanced densification by viscous deformation and thus provides an opportunity to process these composites without pressure.

We are continuing studies on the high resolution imaging of the phase boundaries observed in these composites with the goal of determining the reaction parameters important to the formation of a stable nanocomposite. High temperature mechanical testing has not been done on these materials so the overall stability of these systems is not known. Future studies will principally concern the optimization of the mechanical properties and stability of the composite systems. Other nanocomposite systems involving silicon nitride have been added to this work as well as preliminary studies on the applicability of this procedure to other potential nanocomposite systems (§1.3.1).[26]

1.2.3. Processing of a Mullite Matrix, Molybdenum Disilicide Reinforced Composite

A mullite matrix reinforced with $MoSi_2$ particles was investigated as a potential high temperature composite material.[27,28] Samples containing 2.5 to 20 vol% $MoSi_2$ were processed using both hot pressing and pressureless sintering techniques.[29] Room temperature mechanical testing was performed both in the as-sintered state and after oxidation. Densities of greater than 97% of theoretical were attained for composites containing less then 7 vol% $MoSi_2$ via pressureless sintering. K_{Ic} and strength values of the as-sintered composite were found to be up to two times that of monolithic mullite. After oxidation at 1400°C for 96 hours, the strength improved by 1.5 times over the as-sintered strength, and fracture toughness improved by a factor of 2.5 over the as sintered fracture toughness, indicating that the composite was self-healing during oxidation.

Work in this project focuses on the pressureless sintering process for the production of fully dense composites, using the viscous phase that exists at the particle-matrix interface. High temperature mechanical tests are also planned to determine the suitability of this composite at high temperatures.

1.2.4. Processing of Nanocomposite Powders

The effect of nanoscale inclusions in ceramic monoliths has been reported by Niihara to greatly enhance the strength and toughness of dense ceramics.[30,31] More recently, Wu and Clausen has described enhanced physical properties in SiC/mullite matrix composites, although the intergranular inclusions are hundreds, rather than tens, of nanometers in size.[32] These claims are considered somewhat controversial principally due to the difficulty in synthesizing dense monoliths with uniform distributions of nanoscale inclusions. The results of our own investigations on materials strengthened by the addition of (microscale) inclusions (§§1.2.2, 1.2.3, and 1.3.1) plus our study on chromia and manganese oxide additives in colloidally processed alumina monoliths (§1.2.1) are positive indicators that the processing of powders containing nanoscale inclusions is a viable method for producing such monoliths.

Two processing routes are concurrently under study. One route uses sol-gel processing since powders made from sol-gels sinter to full density at low temperature, as shown in our past work.[33] In the case of mullite, densification is favored by the presence of a viscous phase up to the mullitization temperature (~1250° to 1300°C in TEOS/boehmite sol-gels). Furthermore, we have also shown that mullitization of sol-gels prepared from well-classified boehmite suspensions resulted in the formation of nanoscale silica-rich nanoscale inclusions within the mullite grains. The very fine grains that result from this process yields visibly translucent monoliths that are transparent in the mid-infrared (3-5μm) region of the electromagnetic spectrum.[34]

However, maintaining two phases at high temperature can lead to the concentration of the additive into one phase, encouraging phase segregation and/or the formation of large inclusions in the final powder. These artifacts can be avoided by maintaining chemical homogeneity in the powder. Flash pyrolysis results in dry homogeneous amorphous powders which, in the case of mullite, reduces the temperature of mullitization to ~1000°C.[35,36] Extremely fine grained, highly dense powders result. We believe that the proper processing conditions can result in the precipitation of nanoscale inclusions in these powders and that the precipitation can be controlled using simple thermal treatments. Mullite is very difficult to sinter due to its high creep resistance and this presents a possible limiting factor to the use of powders made using pyrolysis.

Three systems are currently under study: alumina/mullite, chromia/mullite, and titania/mullite. Powders containing varying levels of excess alumina have been made by both the sol-gel and pyrolysis methods. At higher processing temperatures (>1350°C), the resulting powders are similar, consisting of fine grained particles containing small inclusions ~10-20nm in diameter. At lower temperatures (>1000°C) mullitization in the pyrolyzed powders appears complete but the number of inclusions is reduced. XRD results suggest the presence of the second phase at lower processing temperatures in the pyrolyzed powders; high resolution TEM work is required to determine if smaller inclusions can be found within the grains of the powder particles.

Chromia/mullite and titania/mullite powders have been made using the pyrolysis method. Sol-gel procedures have not yet been used with these systems due to the rapid hydrolysis rate of the titania and chromia precursors. As in the alumina/mullite powders XRD characterization indicates the presence of a second phase after mullitization (~1100°C) but microscopic characterization to confirm the morphology of this phase has yet to be performed.

Following the completion of the characterization studies, future work will involve two goals: (i) determining and improving conditions required for the production of mullite powders containing nanoscale inclusions and (ii) using these methods to produce sufficient quantities of powder for densification and sintering studies. Ultimately, we plan to produce test bars from the nanocomposite powders for mechanical testing.

1.3. Ceramic/Metal Composites (<1000°C)

Investigators: ***Yong Li Zhang, Kamal Janghorban, David L. Milius, Mehrdad Yasrebi, Jun Liu, and Ilhan A. Aksay***

1.3.1. Processing of SiC/Al-Si Alloy Laminated and Monolithic Composites

Green compacts of mixtures of alumina and SiC powders have been prepared in our laboratory by colloidal processing.[37] In the next phase of the study, the following two steps were performed: (i) the surface of the SiC particles was oxidized to produce silicon dioxide and to reduce the size of the remaining SiC down to the nanometer scale; and (ii) this was followed by reaction sintering in which a matrix of mullite was produced by reacting the silicon dioxide with alumina, leaving the SiC particles suspended in the matrix material.[38-42]

Alumina and SiC powders were dispersed using PMAA in aqueous solution at high pH in order to obtain high-density green compacts. These suspensions were consolidated by filtration. The densities of the green bodies were 62 to 64% of theoretical density. Reaction sintering was carried out at temperatures ranging from 1550° to 1750°C for 2 or 5h in an argon atmosphere. During sintering the cristobalite phase disappeared and mullite was produced. The quantity of mullite produced depended on the extent of oxidation in the SiC. Moreover, the oxidation treatment was effective in forming high-density sintered bodies. SEM and TEM experiments are now planned to determine the degree of SiC dispersion and the structures of the interfaces.

Liquid metal infiltration in vacuum was successfully used for manufacturing SiC/Al-Si laminated and ceramic matrix monolithic composites . The chemical reactions between SiC and molten Al were studied by TEM.[37] It was confirmed that the formation of Al_4C_3 was through the dissolution of SiC into the liquid Al and then the reaction of SiC with liquid Al. Systematic X-ray diffraction investigations revealed that the amount of silicon in the metal phase and the free carbon content in the SiC powder were two of the main factors that affected the nucleation of

Al_4C_3. The formation of Al_4C_3 was effectively eliminated with 8vol% Si addition. The infiltration was improved to some extent by coating SiC particles with K_2ZrF_6.[43] Strong chemical bonding at the interface provided an excellent combination of strength and fracture resistance. Composites with flexural strength higher than that of fully dense SiC and fracture toughness three times that of SiC were produced. Higher mechanical properties were obtained with SiC/Al-Si laminates, especially the laminate with metal foils between ceramic layers, due to the specific multi-layered structure and shorter infiltration distance resulting in better infiltration.[44] Toughening was apparently due to the ductile phase reinforcement.

From our past work, the following conclusions can be made: (i) In the system of SiC-Al, the formation of Al_4C_3 is through a two- step approach: dissolution of SiC into liquid Al and reaction of SiC with liquid Al. The Si level in the metal phase obviously affects the equilibrium of Al(Si)-SiC-Al_4C_3. The formation of Al_4C_3 is effectively eliminated by alloying Al with Si. (ii) Liquid Al-Si alloy infiltration of SiC in vacuum gives good bonding by mechanical trapping. The strong interface contributes to the good combination of strength and fracture resistance. (iii) Besides ductile phase reinforcement toughening, the specific structural features, the shorter infiltration distance and thus shorter infiltration period, and the versatile possibilities of designing materials are advantages provided by the laminated structure. SiC/Al-Si laminates with continuous metal phase are preferable for higher reliability requirements and higher toughness can be achieved with this structure.

1.3.2. The Wetting Behavior of SiC with Al(Si) Alloys

The effect of silicon addition on the wetting behavior of SiC with Al was evaluated by the sessile drop technique in vacuum. The measurement of the contact angle between SiC substrates and molten Al(Si) showed that at low temperatures there was no apparent difference in the contact angle with or without silicon additions; however, at high temperatures the rate of decrease in the contact angle increased with increasing Si content in the Al(Si) alloy.[45,46] It was also shown that the addition of Si to Al lowered the transition temperature from non-wetting to wetting for the SiC-Al system. EDS analysis indicated spreading and penetration of the Si(Al) alloy on the surface of and into the SiC substrate. A sharper drop in the contact angle was observed in the wetting of Zr containing compound coated SiC with Al(Si) alloy. X-ray diffraction identified the reaction products as ZrSi and AlZrSi.

This study demonstrates the feasibility of making SiC-Al(Si) cermets by liquid metal infiltration in vacuum. Future studies will characterize the SiC-Al(Si) interface through the use of high resolution electron microscopy.

1.4. Methods for Obtaining High Temperature (>1000°C) Ceramic/Metal Composites

***Investigators: Fatih Dogan, John S. Lettow, David L. Milius, and** I. A. Aksay*

To be useful in structural applications it is necessary to engineer metal/ceramic composites to achieve high strength, oxidative resistance, creep resistance, coupled with the low density of the ceramic and the metal's toughness.[30,47-49] The mechanical properties of metal/ceramic composites depend on the properties of the constituents, phase compatibility, and microstructure. For a ceramic matrix containing metallic inclusions, the size, location, and connectivity of the included phase may significantly affect the mechanical properties (i.e., fracture strength) of the composite material.[50,51] The nickel/aluminum oxide system is particularly attractive as a potential high temperature structural material, possibly exhibiting significant improvements over

nickel-based superalloys currently employed in high stress applications (e.g., jet engine turbine components).[52] While the maximum operating temperature of most superalloys is around 1000°C, nickel/alumina composites could potentially operate at temperatures hundreds of degrees higher, with greater creep and oxidation resistances.

Several methods for processing nickel/alumina composites have been developed. Ni/Al_2O_3 composites have been prepared by suspending Al_2O_3 particles in an aqueous solution of $Ni(NO_3)_2$ and adsorbing Ni^{2+} cations onto the surfaces of the particles.[53] Gels fabricated from aluminum alkoxides were used to improve sinterability in powders.[51] NiO powder and α-Al_2O_3 have been mixed in a ball mill and reacted at 1600°C in air for four days to obtain $NiAl_2O_4$. The $NiAl_2O_4$ was subsequently reduced to produce a nickel/alumina composite.[52] These samples were severely cracked due to the large volume difference between $NiAl_2O_4$ and the Ni/Al_2O_3 composite, calculated to be ~19% when going from $NiAl_2O_4$ to Ni/Al_2O_3.[50] However, it has been shown that keeping the size of the nickel inclusions in the reduced samples below ~2μm eliminated cracking in the composite.[50]

Our goal was to develop a viable processing method for producing highly dense Ni/Al_2O_3 composites for testing as high temperature structural materials. Two different means of accomplishing this were studied: (i) reduction of $NiAl_2O_4$ powder and (ii) electrophoretically depositing colloidally dispersed ceramic particles onto a substrate, then coating these with nickel metal through electrodeposition (§1.1.4).

For the thermal method, our first efforts focused on the production of suitable $NiAl_2O_4$ powders for subsequent reduction. A pH of approximately 9.5 was found to be optimum for the precipitation of nickel nitrate from solution. Coprecipitation of NiOH and AlOH (possibly containing AlOOH as well) from a 1:2 ratio of nickel nitrate and aluminum nitrate in aqueous solution at a pH of 9.5 produced an amorphous powder with the appropriate stoichiometry for conversion to $NiAl_2O_4$. With coprecipitation, processing temperatures and times for the formation of $NiAl_2O_4$ were reduced from 1600°C for four days to 900°C for four hours. Additionally, X-ray experiments have revealed that the average crystallite size in the $NiAl_2O_4$ powders converted at 900°C was 13nm. The small size of the nickel aluminate crystallites should facilitate the reduction of the $NiAl_2O_4$ to form nickel/alumina composite powders, the next phase of the study.

The electrical processing route for making metal/ceramic composites involves the electrophoretic deposition of a well packed monolayer of ceramic particles on to an electrode. After deposition the monolayer of ceramic particles is coated with a thin metal layer by electrodepositing metal cations from an aqueous solution. Experiments with high resistivity coated glass electrodes revealed that a thin (~1-2μm thick) layer of nickel metal could be electrodeposited on a ceramic monolayer which was previously formed through electrophoretic deposition of submicron ceramic particles on the electrode (§1.1.4). In regions of the ceramic monolayer well coated with nickel, the nickel deposits completely filled the gaps between ceramic particles and then spread laterally to form a smooth layer over the ceramic particles. On lower resistivity coated glass electrodes, an applied potential of -1.2V with a constant flow of nickel sulfate solution at 0.1μm/min produced regions of smooth but discontinuous nickel deposits. We propose that the electrical process for making nickel/alumina composites could be used to make highly patterned metal/ceramic laminates built up from submicron structures.

2. Functional Ceramics

Barium titanate, $BaTiO_3$, is a ferroelectric material with enormous potential for applications in photonic processing (e.g., optical information storage and optical computation). Because of the current difficulties associated with growing large, inexpensive, optical quality crystals, practical electro-optic or optical-optical switching devices have not yet been produced from $BaTiO_3$ based materials. In order to remedy this situation, the formation of polycrystalline thin films investigated via the synthesis of nanosized $BaTiO_3$ colloid particles, followed by sol/gel processing to produce polycrystalline films and monoliths (§2.1). Grains in these polycrystalline ceramics have to be significantly smaller than the wavelength of light, to minimize internal scattering, so that optically transparency is achieved.

Preliminary work in this area has suggested that the dielectric properties of the resultant film are sensitive to the grain size of the $BaTiO_3$ (§2.2). It is postulated that this effect could either be due to a different crystal domain structure within the particles (as opposed to the crystal domain structure within bulk crystalline material) or, for particles smaller than 10 nm, to quantum confinement (Stark) effects. Although these effects have extremely profound consequences for the performance characteristics of ferroelectric films and monoliths, to date no fundamental study has been performed to measure the dielectric properties of individual $BaTiO_3$ colloidal particles as a function of colloid size. A fundamental understanding of these effects should enable the dielectric properties of the final $BaTiO_3$ films and monoliths to be specifically tailored for required applications (§§2.5 and 2.6).

2.1. Formation of $BaTiO_3$ Particles by Low Temperature (<100°C) Hydrothermal Processing

Investigators: Chang-Min Chun, Fatih Dogan, and Ilhan A. Aksay

We have synthesized nanocrystalline dielectric $BaTiO_3$ particles at 80°C using hydrothermal methods. Since we seek to more fully understand the parameters that control particle size and morphology, our research in this area has been focused on a detailed study of the nucleation and growth of $BaTiO_3$ particles (a general discussion may be found in Nielsen[54]). In part, this has been motivated by the growing commercial demand for uniform particles to be used in applications but, in addition, our previous work has highlighted the conflicts between different mechanisms advanced to explain uniform particle formation. Therefore, our principal goals remain (i) to describe the parameters that control particle size and morphology in hydrothermal processing, and (ii) to determine the mechanism by which particles are formed and aggregate.

$BaTiO_3$ particles were formed from the reaction between nanometer-sized TiO_2 colloids (30nm diameter) $Ba(OH)_2$ (aq) at 80°C. Increasing the $Ba(OH)_2$ concentration was found to decrease the average particle diameter, from 200 nm in 0.46 M solution to 50 nm in 2.23 M solution. No significant difference in particle size (around 40~50 nm) was observed for particles produced at higher concentrations (>2.23 M). The particles were nanosized, spherical, finely divided, monodispersed, and very pure. On the other hand, particles formed at low $Ba(OH)_2$ concentrations (<0.23 M) produced quite different morphologies: the particles were observed to consist of aggregated structures composed of smaller subunits, each ~50nm on edge. Decreasing the $Ba(OH)_2$ concentration increased the aggregate size, from 0.25-0.5 μm in 0.23 M $Ba(OH)_2$ solution to 1.0-2.5 μm in 0.12 M solution.

We determined that the hydrothermal formation of $BaTiO_3$ is controlled by three distinct, but interrelated, processes: (i) Titania first dissolves in the $Ba(OH)_2$ solution, quickly followed by precipitation. (ii) The primary particles aggregate to form the $BaTiO_3$ nuclei. (iii) The $BaTiO_3$

clusters spherodize through the lowering of the total surface free energy via dissolution and recrystallization.

Hertl has proposed that the diffusion of barium ions to the TiO_2 particles is the rate-limiting step in the formation of $BaTiO_3$ particles.[55] This implies that nucleation of the $BaTiO_3$ should be observed at the TiO_2/solution interface. However, we have observed that $BaTiO_3$ nucleates directly from solution, implying that the dissolution of titanium oxide is the determinant in forming barium titanate in the colloidal suspension. This agrees both with the general feature of hydrothermal reactions (solution-based reactions) and with the effect of increasing $Ba(OH)_2$ concentrations and temperature, both of which enhance the solubility of TiO_2. Therefore, the particle size and morphology variation can be explained by considering two competing parameters, the nuclei generation rate and the diffusion rate for aggregation, both of which are limited by the dissolution rate of TiO_2.

The initial primary nuclei are unstable due to their small size (<10 nm), and aggregate although negatively charged (Fig. 7). Because the crystal structure of $BaTiO_3$ is cubic, cubical first generation aggregates with rough surfaces form. The evolution of $BaTiO_3$ illustrates that small $BaTiO_3$ nuclei emerge very early and implies that these particles are present throughout the growth stage. According to Zukoski's nucleation and aggregation model,[56] the critical supersaturation value was exceeded during the complete course of the process and that nucleation proceeded for a substantial fraction of the reaction period. Further studies should demonstrate that nucleation is continuing throughout most of the growth period.

Fig. 7: HREM image of $BaTiO_3$ particles formed within one minute of mixing the precursors. The nuclei precipitate to form an aggregate of crystallites with matching crystal lattices.

Growth by aggregation results in faceted aggregates. The solubility of the small (<10nm diameter) primary particles, particularly at higher pH, encourages spherodization via dissolution and reprecipitation within the $BaTiO_3$ aggregates to form uniform, spherical particles.

We have not yet proven the existence of separate primary nuclei during the formation of $BaTiO_3$ from colloidal TiO_2 particles, nor have we quantified the clustering that leads to the forming of the ultimate particle. Our current research seeks to answer the remaining questions using titanium alkoxides as the titanium source, dynamic light scattering to chart the growth and aggregation of the primary particles, and TEM for adjunct studies on the structure of the particle clusters and the evolution to the final spherical particles found in suspension. These experiments will be used to construct a mechanism to explain particle aggregation with respect to particle formation and the energy of interaction between small particles.

2.2. *Theory of the Size Effect of Small $BaTiO_3$ Particles*

Investigators: ***Wan Y. Shih, Wei-Heng Shih,*, and*** *I. A. Aksay*

* Department of Materials Engineering, Drexel University, Philadelphia, PA 10104.

Bulk $BaTiO_3$ has a ferroelectric transition at $T_c = 122°C$. Above T_c, the crystals are nonpolar and the crystal structure is cubic. Below T_c, the crystals become ferroelectric and the crystal structure changes to tetragonal. However, unlike bulk materials, the $BaTiO_3$ particles made in our laboratory using a hydrothermal approach have diameters ranging from 0.03 to 0.3μm and are *cubic* at room temperature (§2.1). In addition, composites made of these particles in organic polymer displayed enhanced dielectric properties below room temperature.

Ishikawa et al.[57] and Uchino et al.,[58] using Raman spectroscopy and X-ray diffraction respectively, have shown that the cubic-to-tetragonal transition temperature of small $PbTiO_3$ and $BaTiO_3$ particles is size dependent. Arlt et al.[59] and others have shown that the dielectric constant ε of $BaTiO_3$ ceramics is also grain size dependent. The dielectric constant ε was observed to peak at a grain size near 1μm and the peak value is higher than the dielectric constant in either the **a** or the **c** directions. Arlt et al. also showed that in the ferroelectric phase the grains are highly twinned and the twin size decreases with decreasing grain size. They attributed the increase in ε with decreasing grain size to the increasing presence of twin boundaries resulting from a balance between the stress energy within the domains and the twin boundary energy. However, they could not account for the decrease of the dielectric constant at smaller grain sizes.[59]

Our goal is to develop a theory that can explain all of the above phenomena, including: (i) the size dependence of T_c in small particles, (ii) the dielectric anomaly in $BaTiO_3$ ceramics, and (iii) the unusual enhancement observed in the dielectric constant of $BaTiO_3$ particles/polymer composites at low temperatures.

For small particles, surface effects become important. For ferroelectric particles, the important surface effect is the depolarization effect due to the bound surface charge arising from polarization. Therefore, we will consider the effect of depolarization on ferroelectricity. $BaTiO_3$ is not perfectly insulating as a space charge layer will arise to shield the bound surface charge. To accurately account for the depolarization effect in $BaTiO_3$ particles, we must also include the space charge layer effect.

The depolarization energy is reduced through a process by which the small particles form internal domains. The domain size is determined by the balance between the depolarization energy of the domains and the domain-wall energy. The depolarization energy and the domain wall energy will be incorporated into the Landau-Ginsburg expression for free energy which is known to be a good description of the ferroelectric transitions in large single crystals. The domain-wall energy can also be put within the framework of the Landau-Ginsburg free energy by assuming a hyperbolic tangent polarization profile at the domain wall. The domain-wall energy and the domain-wall width for a given domain polarization can be obtained by minimizing the domain-wall energy with respect to the domain width. So, for a given particle size and a given temperature, the free energy (a function of the polarization P and the domain size D) will be minimized with respect to P and D to obtain the equilibrium values of both P and D.

Our results to date have shown that both the domain-wall energy and the domain-wall width are in good agreement with the literature values. We have also shown that the ferroelectric transition temperature T_c decreases with a decreasing particle size, in agreement with the XRD and Raman experiments of Ishikawa et al. and Uchino et al. The domain size decreases with

decreasing particle size (Fig. 8), in agreement with the TEM observation of Arlt et al.[59] Finally, due to the size dependence of T_c at a given temperature, the dielectric constant peaks at a certain size (Fig. 9), again in agreement with past and current observations.[60]

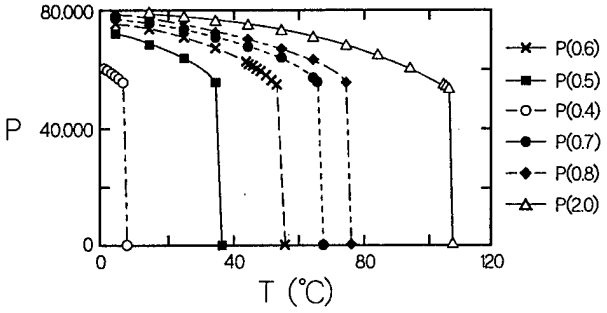

Fig. 8: The change in the ferroelectric transition temperature Tc as a function of particle size.

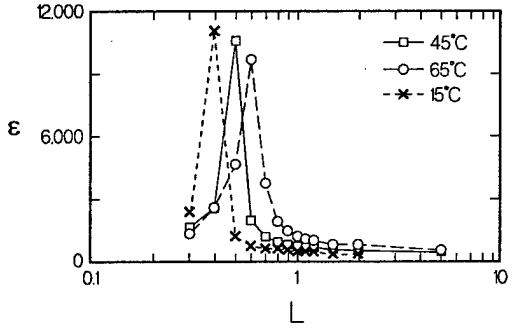

Fig. 9: Because of the size dependence of Tc at a given temperature, the dielectric constant ε peaks at a certain size L of the particles.

2.3. Low Temperature (<500°C) Processing of PZT Thin Films Through Seeding
Investigators: W. David Clifton, Fatih Dogan, and Ilhan A. Aksay

This study involves forming thin films of the ferroelectric material lead-zirconate-titanate ($PbZr_{0.52}Ti_{0.48}O_3$, PZT) onto the direct gap III-V semiconducting material GaAs. Direct gap semiconductors have been envisioned for use in a high speed optical computer which can operate at speeds several orders of magnitude greater than current silicon based electronic computers.[61] Development of these computers is hindered by the production of a material which can switch light at the high operating speeds desired of this new computer. Thin films of PZT have the potential of achieving the necessary high switching speeds for both light and electronic signals. This switching is only possible in the ferroelectric tetragonal perovskite crystal assemblage of PZT. Unfortunately, to develop the perovskite phase within the film normally requires processing at 650°C, a temperature which destroys GaAs.[62-64] If a thin film of perovskite PZT can be produced below 400°C, the coupling of PZT and GaAs would be possible. This temperature reduction is the goal of this study.

To date, our work has isolated several problems which hinder the crystallization of the perovskite PZT phase at temperatures around 400°C and we have partially solved the crystallization temperature problem based on our observations. All current wet chemical techniques used for the deposition of PZT films require processing at 650-700°C to fully crystallize the perovskite phase. These films are initially amorphous after deposition and upon heating they first crystallize into an undesirable pyrochlore phase above 475°C followed by very slow crystallization of the perovskite phase. Lower temperature perovskite formation is hindered by the high perovskite nucleation temperature (>525°C) and the low density of perovskite nucleation sites (1-5 sites/100 mm^2), requiring long growing times for complete perovskite phase transformation.

We have prevented pyrochlore formation by depositing a monolayer of 100-200nm perovskite PZT 52/48 particles onto the substrate surface onto which we then spin coat a film of PZT 52/48 precursor solution. The perovskite particles act as nucleation sites for the perovskite phase and thus seed the growth of the perovskite.[65] Upon heat-treatment, the seeded films

crystallize directly from the amorphous state to the perovskite phase at 460°C, completely circumventing the formation of the pyrochlore phase. Electrical property measurements of the low temperature seeded films indicated that they have a dielectric constant of over 700 and a remnant polarization of 11 mC/cm^2, while unseeded films have to be heated to 700°C to have similar properties. With these encouraging results, our future research will emphasize greater reductions in the perovskite crystallization temperature along with attempts to place PZT films onto GaAs substrates.

2.4. Piezoelectrical Properties of $Pb(Zr_{0.52}Ti_{0.48})O_3$ Sintered at Low Temperature

Investigators: Fatih Dogan and Ilhan A. Aksay

Nb-doped PZT powders containing excess PbO have been prepared by coprecipitation from metal-nitrate solutions followed by freeze-drying. We have found that if, prior to freeze-drying, the precipitate is washed free of nitrates and then dispersed in a suitable solvent the formation of agglomerates could be controlled. Powders can be compacted without milling to a narrow nanometer-sized pore distribution and then sintered at 750°C to 98.5% of theoretic density. Evaporation of PbO during sintering is significantly reduced. For low temperature sintering, a diffusion-controlled mechanism has been proposed based on the high vapor pressure of PbO at lower temperatures.

Samples are thickness mode resonant from 1.5 to 1.75 MHz. The capacitance of the sample measured at 1 kHz gives a good estimate of the free dielectric constant and its associated loss tangent. Electrical impedance magnitude and phase were used to identify the thickness resonance frequencies f_s and f_p in order to calculate the electromechanical coupling coefficient k_t. Dielectric and piezoelectric properties are summarized in Table 1.

Sintering Temperature	800°C	1000°C
Dielectric Const. (@ 1 kHz)	501	622
Loss Tangent	0.032	0.044
Coupling Coef. k_t	<<	0.55

Table 1. The sample sintered at 800°C shows no resonance peaks, thus exhibiting no measurable piezoelectrical activity. In contrast, a sample sintered at 1000°C exhibits normal resonance characteristics and piezoelectrical activity comparable to commercial PZT. The loss tangents are within normal bounds.

The improvement of piezoelectrical properties has been usually attributed to the increased grain size.[61,62] In this study, no significant difference in grain size was observed between the samples sintered at 800°C and the samples sintered at 1000°C. Detailed microstructural characterization is necessary to determine the influence of grain boundary composition, development of tetragonal perovskite structure, and domain formation on the piezoelectrical properties. The calcination temperature has been shown to affect the sintering behavior and dielectrical properties of the samples. Powder (from a different batch as described above), calcined at 400°C resulted in 80.6 % of theoretic density after sintering at 800°C. Sintering density of >95 % theoretic density was obtained when the powder was calcined at 600°C. This may be attributed to the pyrochlore phase which forms at low calcination temperatures. The

phase transformation during heat treatment can alter the pore structure of the compacts due to the density differences between the pyrochlore and perovskite phases.

The dielectric constants (@ 25°C) of the samples calcined at 400°C and 600°C were ~500 and ~700, respectively. At the curie temperature the dielectric constants were 2100 and 4400 for low and high temperature calcined samples respectively. This behavior is attributed to the significant difference in the respective porosities of the samples as it is known that increasing porosity results in decreasing dielectric constant.[61]

2.5. Pressure Filtration of Hydrothermal $BaTiO_3$ Powder

Investigators: Fatih Dogan and Ilhan A. Aksay

Lowering the sintering temperatures of $BaTiO_3$ is necessary for reasons of economic processing in addition to maintaining material properties.[66] Lower sintering temperatures permit the use of low cost electrode materials having low melting temperatures in the manufacture of multilayer capacitors. Further, novel material properties are expected through better microstructural control, such as in making transparent materials for optoelectronic applications. Our long term goal is the processing of polycrystalline transparent $BaTiO_3$; our approach uses low sintering temperatures by reducing the grain size. To achieve highly dense green compacts with narrow pore size distribution colloidal processing and pressure filtration techniques are required.

The use of fine $BaTiO_3$ powders with particle size <0.1 μm should succeed in preparing fine-grained (<0.3 μm) $BaTiO_3$ monoliths under the correct conditions. We can control the average particle size of powders between 0.01 μm and 1 μm by adjusting the process parameters during hydrothermal processing. Sintering densities of up to ~99% of theoretical density have been achieved at 1225°C using dry pressed compacts. In these samples, the grain size was reduced to 0.4 μm using 0.9 wt% Nb addition.

Preliminary dispersion studies on $BaTiO_3$ in aqueous and nonaqueous solvents have revealed that the particles can be dispersed and sterically stabilized in water using PAA as the dispersant and at a suspension pH of 9. Pressure filtration of sterically stabilized suspensions formed crack-free compacts (25 mm diameter by 5 mm thick). A highly concentrated acetate-based precursor of $BaTiO_3$ was used as dispersant to achieve *in situ* infiltration of the compacts during pressure filtration. This approach enables infiltration of bulk samples without forming concentration gradients.

Continuing studies on the pressure filtration of $BaTiO_3$ suspensions will be done with and without the addition of niobium as sintering aid. The role of niobium in controlling the grain size will be investigated using high resolution electron microscopy. The green and sintered densities of pressure-filtered samples will be compared with those of dry-pressed samples. To achieve yet higher packing densities, nanometer-sized particles (§1.1.2) will be pressure filtered. This will eliminate the drying step and thus the concomitant agglomeration of nanometer-sized particles.

2.6. Low Temperature Processing of $BaTiO_3$ Thin Films

Investigators: Fatih Dogan and Ilhan A. Aksay

The fabrication of $BaTiO_3$ thin films by conventional techniques, such as the use of sol-gels, requires high temperature heat treatments (>1000°C) mainly due to formation of $BaCO_3$ as an intermediate reaction product which decomposes above 900°C. Because of the high processing temperatures, controlling of the grain size is difficult, especially when small grain sizes are

required. For the same reason, the selection of substrate materials is limited. Crystalline $BaTiO_3$ has been prepared at low processing temperatures (<200°C) through the reaction of a titania precursor and barium hydroxide solution (§2.1). Thermodynamically, the synthesis of $BaTiO_3$ at room temperature is possible.[67,68] The reaction is, however, kinetically favored above 50°C. Our goal is to prepare dense and crack-free $BaTiO_3$ thin films at low processing temperatures so that a variety of substrate materials can be used in the fabrication of optoelectronic devices and composites.

Sputtering titanium onto a substrate is a common technique used to form a continuous metal precursor layer prior hydrothermal treatment in $Ba(OH)_2$ solution.[66,69] Our titanium precursor films were prepared by sol gel process and spin coating of metalloorganic compounds having very slow hydrolysis rates (such as titanium diisopropoxide bis(2,4-pentanedionate)). The slow hydrolysis permits the formation of crack-free and transparent coatings after drying. Polystyrene and glass substrates were chosen due to their respective stability when exposed to strong bases at high temperature. The substrates were hydrothermally treated at 80°C to form crack-free, continuous transparent films composed of densely packed particles less than 0.1 μm in size. XRD analysis could not distinguished between cubic and hexagonal phases in the film.

The formation of the film is thought be via a mechanism of dissolution and precipitation as described for the formation of nano-sized particles. Experiments to confirm this model and the role of processing parameters in the production of fine grained thin films are continuing.

3. Model Systems

3.1. Formation and Sintering in Nanometer Size Particles

Investigators: Wan Y. Shih, Wei-Heng Shih,* Daniel M. Dabbs, Nan Yao, and Ilhan A. Aksay

*Department of Materials Engineering, Drexel University, Philadelphia, PA 10104.

Past studies within earlier AFOSR-sponsored projects have use gold particles for model studies on the formation, agglomeration, packing, and sintering of nanometer-sized particle suspensions. As determined by our group in earlier and on-going studies (§3.2),[70,71] the growth of necks between touching particles falls into two kinetic regimes, the first in which the neck diameter scales with the cube root of the sintering time, the second in which the neck diameter scales with the square root of the sintering time . Our preliminary model relates this observation to the relative sizes of the domains within the particles in contact and the neck diameter (based on pore elimination models). We have further proposed that sintering between nanometer-sized particles is due to a form of viscous phase sintering since discrete boundaries were not observed between the particles.

3.1.1. Surfactant Mediated Deformation of Gold Agglomerates

In addition to the sintering of gold particles, we have observed the apparent surfactant driven "desintering" of ramified gold agglomerates. Using the method of Turkevich et al.,[72] we have made suspensions of nanometer size gold particles from mixtures of sodium citrate (aq) and gold chloride (aq). The formation process can be divided into three distinct stages: (i) In the first stage, nuclei of about 2nm in diameter form and aggregate to form large clusters. ζ-potential measurements showed that adsorption of the negatively charged citric ions onto the gold surface continued during this stage. The duration of the first stage was short, less than one minute at 90°C. The surface was soon saturated with citric ions and the size of the clusters stabilized. (ii) In

the second stage, the clusters undergo extensive restructuring, leading to the breakup of the clusters into smaller gold particles. (iii) In the third stage, the gold particles reach a uniform size and remain stable in the suspension.

Fig. 10: (a) Ramified gold agglomerate with twin domains (domain size<10nm). (b) Final gold particles (~24nm average diameter).

We established that the negatively charged citric ions adsorbed on the gold surface were the principal components in the reaction mixture which determined the size of the final spherical particles seen at the end of stage (iii). The adsorption of the ions set the total electrostatic surface energy on the gold and the magnitude of the gold-water interfacial tension. The minimization of the total surface energy then set the final size of the gold particles. We have shown both theoretically and experimentally that the gold particle size is proportional to $(C_c/C_{Au})^{2/3}$, where C_c is the citric acid concentration and C_{Au} is the concentration of gold ions in solution.[70]

However, during the second stage of particle formation, we have recently observed that ramified clusters formed from the sintering of nanometer size nuclei formed in stage (i) (Fig. 10).[73] These structures were multiply twinned into domains smaller than 10 nm and eventually broke up to form the final spherical particles. This breakup involves desintering or "dewelding"[74] from the continuous agglomerate to form the distinct particles.

The goals of this research topic are to (i) establish the mechanism of desintering and (ii) determine the effect of surface modifications on desintering and sintering.

Spectroscopic studies of citrate-stabilized gold suspensions have been done using attenuated total reflectance (ATR) infrared spectroscopy. As shown in Fig. 11, significant changes in the spectrum of the citrate result from its interaction with the gold particles. First, the strong presence of the two anti-symmetric and symmetric stretching modes at ~1550 and ~1400 cm^{-1} and the absence of significant absorption between 2500-3000 cm^{-1} in the citrate solution spectrum indicates that sodium citrate is completely dissociated in solution. Once gold particles have been formed, the spectrum shifts markedly. The presence of bands near 2860 cm^{-1} and 1700 cm^{-1} indicate the presence of saturated carboxylate ions, supported by the pronounced decrease in the ~1550 and ~1400 cm^{-1} bands. Absorbance bands now appear at 1150 and 1200 cm^{-1}; their location corresponds to the presence of hydroxides unencumbered by hydrogen bonding.

In terms of ultimate stability, the rod-like structures in the intermediate stage is unstable against the formation of spherical particles. It is known that the negatively charged citric ions

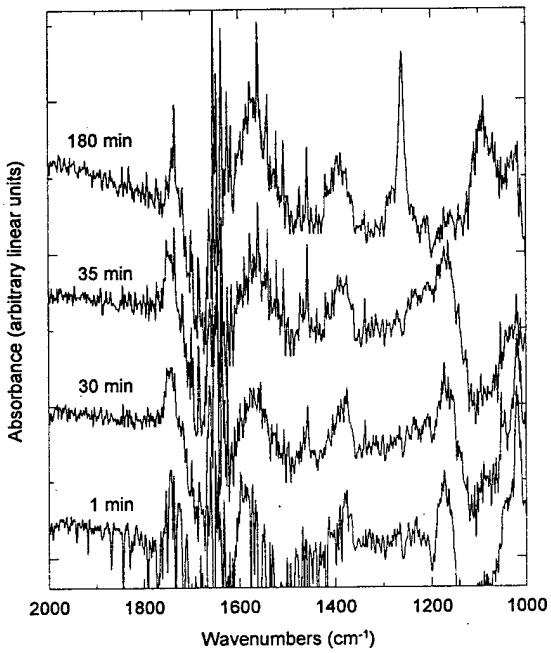

Fig. 11: ATR spectra for (i) sodium citrate in aqueous solution and (ii) gold particles stabilized by citrate ions in aqueous suspension.

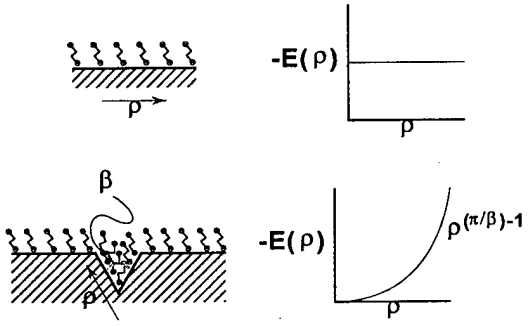

Fig. 12: Smooth metal surface with constant potential (top) and surface containing cusp of low potential (bottom). The high density of adsorbates within the cusp forces migration of metal atoms from the apex, sharpening the cusp and eventually leading to separation.

have already adsorbed on the gold surface. With surface charges, the rod-like structures observed in the intermediate stage have a high electrostatic energy than spherical particles.

Due to the adsorbed citric ions, the electrostatic energy not only influences the final particle size and shape but also governs the dewelding process. For example, let us consider a flat metal surface with a constant potential as illustrated in Fig. 12. On such flat surface, the formation of a corner is favored because the electric field is diminishing at the corner. The narrower the corner the more stable the corner. As driven by this electrostatic stability, the corner will become sharper and sharper until the rod breaks up, which is observed in our TEM micrographs. The dewelding phenomenon is the sharpening of the corners.

To facilitate the sharpening of the corners, gold atoms must be able to move around. It is well known surface atoms can have much higher (often several orders of magnitude higher) mobility than bulk atoms. The enhanced mobility of the gold atoms in these nanometer-size rods to facilitate dewelding is conceivable: (i) the diameter of the rods is on the order of 10 nm, therefore, a high percentage of atoms are on the surface. (ii) These rods are highly twinned. Each crystalline domain (likely separated by twin boundaries) is smaller then 10 nm. The high population of the domain boundaries also contributed to the high mobility of gold atoms in these rods. The other evidence is that each corner is connected to a domain boundary.

To conclude, the dewelding phenomenon observed in these gold rods is a process (a) driven by the minimization of the electrostatic energy and (b) facilitated by the high mobility of the gold atoms in these structures. The high mobility is attributed to the extensive presence of crystalline domain boundaries and the high surface area of these rods.

3.1.2. Neck Formation of Nanometer Sized Particles

Preliminary experimental observations of the necking between two nanometer size gold particles showed that the neck size L increases with time t as $L \propto t^{1/3}$ at small t and as $L \propto t^{1/2}$ at large t. Our previous simulations on single-pore elimination in a polycrystalline matrix also showed two scaling regimes:[7575] for small pores, the pore elimination time t_p scales with the

initial pore radius r as $r \propto t_p^{1/3}$ and for large pores, $r \propto t_p^{1/2}$. The crossover from $r \propto t_p^{1/3}$ to $r \propto t_p^{1/2}$ corresponds to a pore radius r that is approximately equal to the grain radius G.

We have observed that small gold particles are usually multiply twinned into about five or six domains as seen in TEM micrographs (Fig. 13). Therefore, we think that the observation of two scaling regimes in the neck formation between two nanometer-sized gold particles is a result of crossover from one regime where the neck is smaller than the domain size to another where the neck is larger than the domain size, analogous to the presence of two scaling regimes in single pore elimination. Thus, our objective in this portion of the project is to explain the observed crossover from one scaling regimes to another in the neck formation in nanometer sized gold particles.

Fig. 13: Necking between nanometer sized particles.

Our approach consists of two parts: computer simulations of the necking process and scaling analysis. In the first, simulations are performed using a model we previously developed capable of modeling both orientational flipping and diffusion. Orientational flipping gives rise to grain growth and diffusion gives rise to sintering. The model is capable of displaying various sintering phenomena such as densification, the growth of large pores, pore coalescence, pore shrinkage, evaporation and condensation, thermal etching, rounding of a sharp corner, and necking. In this study, we are looking at the neck formation between two spherical particles each containing five to six domains of different crystalline orientations.

The results of our scaling analysis to date have shown that the neck size indeed goes as $L \propto t^{1/3}$ for L smaller than the domain size G and as $L \propto t^{1/2}$ for L larger than G. The difference in the scaling behavior between the region where L is smaller than G and the region where L is larger than G is a function of the total area of the intersecting domain boundaries. In the region where $L > G$, the total area of the domain boundaries intersecting the neck region is given by L^{d-1}/G, where d is the Euclidean dimension. Where $L < G$, the total area of the domain boundaries intersecting the neck region is L^{d-2}. The scaling laws have been shown to be independent of the dimensionality.

3.2. Mesoporous Silicate and Aluminosilicate Materials

Investigators: ***Michael D. McGehee, Sol M. Gruner, Nan Yao, Chang-Min Chun, Alexandra Navrotsky, Itaru Honma, Thara Srinivasan, and Ilhan A. Aksay***

The synthesis of materials with nanoscale (1-100 nm) pores and pore structure is important to a host of applications including catalysts, ultrafiltration, protein stabilization and characterization, and separation technology. Microporous materials are usually crystalline framework solids (such as zeolites) whose pore dimensions formed are in a range of 10-15Å. Recent work by Mobil scientists have revealed a surfactant-based procedure which yields mesoporous silicate/aluminosilicate materials with pores up to 10nm in size arranged in either lamellar, hexagonal, or bicontinuous cubic structures.[76,77] Two different models have been proposed to explain the formation of these materials: either (i) the mineral precipitates onto the

exposed surface of a water-surfactant liquid crystal phase or (ii) the condensation of the mineral acts in concert with the crystallization of the surfactants to form the ordered structure (co-assembly). Our work using time-resolved X-ray diffraction show that transitions between the structures occur during synthesis, supporting the co-assembly model. We have also demonstrated that the morphology of the co-assembled phase can be controlled and have begun to apply these materials to coating and nanocomposite processing.

3.2.1. Self Assembling Mesoscopic Materials

Cubic surfactant-silicates were synthesized by mixing tetraethoxysilane (TEOS)with Arquad (a proprietary surfactant), NaOH, and water. The TEOS dispersed into the surfactant solution and hydrolyzed. Heating resulted in the formation of solid particles. The surfactants were removed from the particles by calcination at low temperature to preserve the pore structure.

X-ray diffraction (XRD) and TEM analyses showed that the particles had an Ia3d cubic symmetry before and after calcination, but that the lattice parameter shrank from 97 to 84Å as a result of the densification. Fig. 14 shows examples of the lamellar, cubic, and hexagonal surfactant-silicates made by similar methods, but with different chemical ratios of reactants.

Fig. 14: TEM images of (a) the lamellar morphology, (b) the cubic phase with Ia3d symmetry viewed along its [111] zone axis, and (c) the hexagonal phase viewed along its [001] zone axis (bars = 30 nm).

The formation of cubic surfactant-silicates was studied with time-resolved XRD using a specialized X-ray beamline.[78,79] Three distinct phases were observed during reaction (Fig. 15). The first phase had an XRD pattern with only one broad peak and could not be identified (Fig. 15a). This phase persisted for weeks in synthesis solutions which were kept at 20°C, but was replaced by the second phase within 30min at 100°C. The second phase had a 2-peak XRD pattern (Fig. 15b) which was consistent with a lamellar morphology having a 35 Å repeat distance. The third phase had an XRD pattern (Fig. 15c) consistent with Ia3d symmetry. Transformation from the lamellar to cubic phase has been observed as the Ia3d cubic mesophase growing epitaxially from the lamellar phase. Controlled phase morphology is achieved by using slightly different surfactant groups and coassembling the surfactant and silicates into the desired structure. Although questions remain about the mechanism of coassembly, the knowledge that we can control the microstructure permits work on the applications of mesophase materials, described in the following sections (§§3.2.2 and 3.2.3).[80]

3.2.2. Thin Film Formation of Mesoporous Silicate

Mesoporous materials now include titanium silicate, antimony oxide, tungsten oxide, iron oxide, lead oxide, and zinc oxide.[81,82] The self-organized regular array structure of the mesoporous channels is formed through the replication of the liquid crystal templating (LCT) phase of the surfactant/water system. Depending on the LCT structure, lamellae, hexagonal, cubic crystalline phase particles can be precipitated homogeneously in the solution (§3.2.1). For

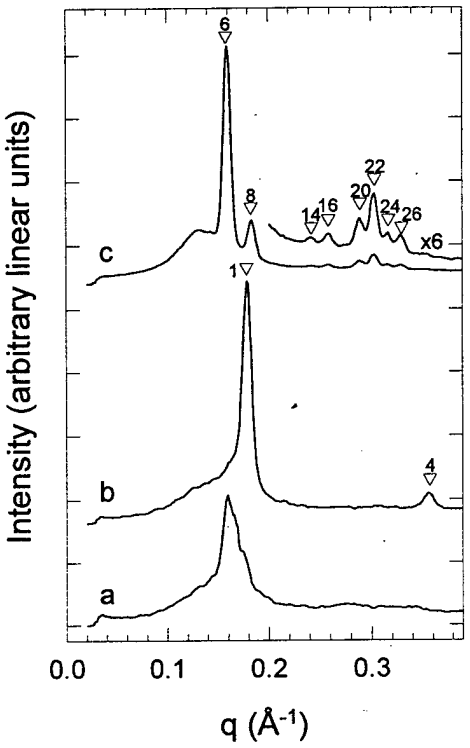

Fig. 15: XRD patterns from a time-resolved experiment. The numbers with the peak labels are the square of the peak indices. (a) 20min exposure taken during the first 20 min of heating. (b) 20min exposure taken after 160 min of heating. The two peaks are consistent with a lamellar structure, as shown by the peak labels. (c) The average of six 20min exposures taken after 20 h of heating. The 8 peaks are consistent with Ia3d symmetry, as shown by the peak labels. There were two faint rings at higher q which did not match the Ia3d pattern and are not explained.

applications involving chemically functionalized surfaces, a method for forming continuous and homogeneous films onto substrates would be a valuable tool. Ceramic thin-film formation on functionalized interfaces mimics biological processes responsible for forming natural composites such as teeth, bones and shells.[83] By manipulating the nucleation and growth on the functionalized interface, the films can be formed at ambient temperatures. The important parameters controlling formation appear to be the proper combination of solution chemistry and surface functionalization.

In general, we have observed that as the surfactant/TEOS ratio is decreased, the solution condition moves from the particle precipitation region to the film formation region. In the system used in this study, a four-fold dilution of the concentrated particle-precipitated solution can be used to form continuous films on substrates such as Mylar or glass. As water is removed the film forms as a white gel. Subsequent hydrothermal processing results in a rigid transparent glass. XRD and TEM studies showed that the obtained film structure consists of a disordered mesophase containing small inclusions of a crystalline phase. The mesophase has short range ordering of ~40-45Å, equivalent to the d-spacing of both the lamellae and hexagonal phase, but lacks long range ordering. This is probably related to the phase behavior in the biosurfactant/water system. Dilution can shift the equilibrium solution phase from hexagonal to disordered hexagonal/lamellae and, as a result, the film consists of the disordered mesostructure phase largely because the film structure replicates the LCT structure of the biosurfactant. Additionally, the seeding of crystalline particles onto the substrate did not enhanced the crystalline film growth indicating that modifying the substrate surface does not prevent the disordering of the film simply because the deposited film structure is primarily determined by the structure of the solution.

We have found that the film structure is closely related to the phase behavior of the surfactant/water system. The key goal in this work is to find the appropriate conditions under which the solution surfactant/silicate structure remains in crystalline hexagonal region and the film forms onto the substrate without particle precipitation. If transparent and continuous films can be successfully prepared on the substrate, new application are envisioned through the chemical and physical infiltration of functionalized molecules, clusters and small particles, dyes, and proteins into the mesoporous channels. Because of the potential advantage of uniformity of the pores, high doping ratio, and uniform orientation of the channels, such films can be used to form optical non-linear devices, high dielectric capacitors, separation membranes, and templated supports for nanocomposites.

3.2.3. Fabrication and Characterization of Mesosilicate Nanocomposites

Several synthesis routes are under investigation for fabricating nanocomposites using mesoporous materials. Second phase materials include: (i) metal alkoxide precursors (ceramic/ceramic composites), (ii) organic monomers, and (iii) metals. Once infiltrated, larger potentially more useful materials can be formed from the resultant nanocomposite powders. As described in the preceding section (§3.2.2), thin film formation is currently under investigation. Continuous mesoporous films offer a suitable substrate for the formation of nanocomposite layers that might be built up to form larger and/or graded materials. Further, chemical modification of the pore surfaces may be used to both stabilize the mesoporous structure and enhance the infiltration of the pores by the appropriate second phase precursor.

Attempts to infiltrate the mesoporous silicate with metal alkoxides has had mixed results. Using a technique developed for the infiltration of wood cell walls by alkoxides (§3.3), it was determined that slower hydrolyzing alkoxides achieved higher penetration depths. Infiltration by TEOS resulted in up to 40% of the pore volume being filled with silica gel. However, the more rapidly hydrolyzing aluminum and titanium alkoxides merely coated the outside of the mesoporous powder. In the coassembled materials, the surfactant is believed to act as a steric barrier to infiltration by organometallics; when the surfactant is removed, the high hydroxyl content on the pore surfaces favors hydrolysis and condensation and penetration is blocked by the plugging of the pores by the resulting ceramic or gel. Hydrolysis of the organometallic can be slowed by the use of larger functional groups on the metal cation but steric hindrance is enhanced and infiltration is not improved.

We have shown that suitable organics can infiltrate the mesostructure. A zwitterionic monomer can be inserted into the pores and then polymerized *in-situ* to form a ceramic/polymer composite. BET surface sorption and TGA measurements indicate that the polymer coats the pore surfaces although the uniformity of this coating has not been determined. Effective surface areas in the mesoporous material were reduced from $576 m^2/g$ for the calcined material to $17.0 m^2/g$ in the infiltrated material.

Finally, metal infiltration has been attempted using a two step process: (i) solution infiltration by aqueous solutions of metal salts and (ii) reduction of the metal ions in the pores. The resulting materials are highly colored but we have not yet shown the formation of nanoscale metal particles within the mesostructure.

Current studies emphasize the role of the surface to the successful infiltration of the mesostructure by precursors or precursor solutions. Subsequent processing conditions, such as the method used to reduce the metal cations to metal, must be designed so as to optimize the retention of the second phase while preventing the collapse of the mesophase.

3.3. The Formation of Ceramic/Cellulose Cellular Composites

Investigators: Sara E. Keckler, Daniel M. Dabbs, Nan Yao, and Ilhan A. Aksay

Cellular organic structures such as wood can be used as scaffolds for the synthesis of complex structures of organic/ceramic nanocomposites. The wood cell is a fiber-reinforced resin composite of cellulose fibers in a lignin matrix. A single cell wall, containing several layers of different fiber orientations and lignin content, is separated from its neighboring wall by the middle lamella, a lignin-rich region.[84] In order to achieve total mineralization, deposition on and in the cell wall must be achieved.[85] Geological fossilization of wood occurs as permineralization (filling the void spaces with mineral) and petrifaction (mineralizing the cell wall as the organic

component decays) through infiltration of wood with inorganics after growth.[85] Conversely, living plants can incorporate inorganics into their cells and in some cases into the cell walls during growth.[86] This project has involved attempts to mimic geological fossilization via infiltrating inorganic precursors into wood cells; by doing so we hope to enhance the physical properties of the wood.[87] Our most current work has used electron microscopy and vibrational spectroscopy to study the structure of silica formed in the cell walls after infiltration of the cell walls by tetraethoxysilane (TEOS).

Partially hydrolyzed TEOS in ethanol (25% by volume) was infiltrated into rehydrated kiln-dried lumber samples of hemlock and pine. Impregnation was completed in a partially evacuated reaction chamber at room temperature. After curing for two days at 105°C, the impregnated samples were heat treated at temperatures between 200° and 600°C to fully convert the precursor to silica and to remove part or all of the organic matrix. Electron micrographs reveal that the structure of the wood cell is unaffected by the presence of silica (in the form of silica gel). Energy dispersive spectroscopy (EDS) measurements confirm the presence of silica gel across the cell wall prior to heat treatment. Infrared spectroscopy revealed that the formation of the silica gel is preferential within the cell wall. Binding between the gel precursors and the organic component of the cell wall is seen in the formation of C–O–Si bridges within the cell wall; these bridges decay with increasing temperature and the loss of the organic phase.[88]

Two forms of silica are found within the cell wall: (i) particles on the wall bordering the middle lamella and (ii) dense uniform silica gel in the bulk of the cell wall. The pH of wood extractant is around 4.6 suggesting that the silica on exposed surfaces results from acid-catalyzed hydrolysis and condensation of TEOS. This is indicated by the particulate nature of silica observed at the boundary layer. The bulk silica is finer in texture than the boundary layer silica. We attribute the finer bulk texture to the geometrical constraint imposed on the polymerization of silica within the inter-cellulosic confinements of the cell wall. Before and after the removal of the organic phase by pyrolysis, the gross cellular structure of the wood is maintained, replicated on the micron scale by silica (Fig. 1).[88]

Fig. 16: SEM micrographs of infiltrated wood (a) before pyrolysis and (b) after pyrolysis at 600°C. The wood's cellular structure has been replaced by silica in (b).

References:

1. T. S. Yeh and M. D. Sacks, "Low-Temperature Sintering of Aluminum Oxide," *J. Am. Ceram. Soc.*, **71** [10] 841-44 (1988).
2. G. C. Bye and G. T. Sipkin, "Influence of Cr and Fe on Formation of α-Al_2O_3 from γ-Al_2O_3," *J. Am. Ceram. Soc.*, **57** [8] 367-71 (1974).
3. M. Kumagai and G. L. Messing, "Enhanced Densification of Boehmite Sol-Gels by α-Alumina Seeding," *J. Am. Ceram. Soc.*, **67** [11] C-230-31 (1984).
4. M. Kumagai and G. L. Messing, "Controlled Transformation and Sintering of a Boehmite Sol-Gel by α-Alumina Seeding," *J. Am. Ceram. Soc.*, **68** [9] 500-05 (1985).
5. D. S. Horn and G. L. Messing, "Alumina Monolith Formation by Flocculation of Boehmite Sols," *J. Am. Ceram. Soc.*, **72** [9] 1719-21 (1989).
6. I. A. Aksay and C. H. Schilling, "The Mechanics of Colloidal Filtration," in *Forming of Ceramics, Advances in Ceramics*, Vol. **9**, edited by J. A. Mangels and G. L. Messing (American Ceramic Society, Columbus, Ohio, 1984), pp. 85-93.
7. C. H. Schilling, W.-H. Shih, W. Y. Shih, and I. A. Aksay, "Advances in Drained Shaping of Ceramics," *Ceramic Powder Science IV, Ceram. Trans.*, Vol. **22**, edited by S. Hirano, G. C. Messing, and H. Hausner (American Ceramic Society, Westerville, Ohio, 1991), pp. 307-20.
8. R. A. Shelleman, G. L. Messing, and M. Kumagai, "Alpha Alumina Transformation in Seeded Boehmite Gels," *J. Non-Cryst. Sol.*, **82**, 277-85 (1986).
9. I. A. Aksay, "Molecular and Colloidal Engineering of Ceramics," *Ceramics International*, **17**, 267-74 (1991).
10. K. T. Miller and C. F. Zukoski, "The Osmotic Consolidation of Suspensions and Gels," *J. Am Ceram. Soc.* **77** [9] 2473-8 (1994).
11. R. D. Bagley, "Extrusion Method for Forming Thin-walled Honeycomb Structures," U.S. Patent #3,790,654.
12. I. M. Lachman, *et al.*, *Am. Ceram. Soc. Bull.*, **60** 202 (1981).
13. R. R. Tummala, *IBM J. Res. Develop.* **36** 817 (1992).
14. T. C. Halsey, *Science* **258** 761-766 (1992).
15. C. F. Zukoski, *Ann. Rev. Mater. Sci.* **23** 45-78 (1993).
16. A. P. Gast and C. F. Zukoski, *Adv. in Colloid and Interface Sci.* **30** 153-202 (1989).
17. R. Newnham and G. R. Ruschau, *J. Am. Ceram. Soc.* **74** 463 (1991).
18. I. A. Aksay, *et al.* (Eds.) *Hierarchically Structured Materials, MRS Proc.* **255** (1992).
19. R. Lakes, *Nature* **361** 511-515 (1993).
20. K. A. Lurie and A. V. Cherkaev, *Proc. Roy. Soc. Edinburgh* **99A** 71 (1984).
21. S. Torquato, *Appl. Mech. Rev.* **44** 37-76 (1991).
22. F. F. Reuss, "Notice sur un novel effet de l'eletricite galvanique," *Mem. Soc. Imp. Natur. Moscov*, **2** 327-37 (1809).
23. "Advanced Ceramic Processing and Technology" **Vol. 1**, J. G. P. Binner, ed.(Noyes Publications, Park Ridge, New Jersey, 1990).
24. R. C. Bradt, "Cr_2O_3 Solid Solution Hardening of Al_2O_3," *J. Am. Ceram. Soc.* **50** [1] 54-55 (1967).
25. Y. Sakka, D. D. Bidinger, and I. A. Aksay, "Processing of SiC-Mullite-Al_2O_3 Nanocomposites," *J. Am. Ceram. Soc.*, **78** (1995).

26. Y. Sakka and I. Aksay, "Processing of Nanocooomposite Silicon Nitride-Mullite-Alumina By Reaction Sintering," *NanoStructured Materials*, **Vol. 44**, No. 2, pp. 169-182, (Elsevier Science Ltd. Pergamon, 1994).
27. M. P. Borom, M. K. Brun, L. E. Szala (GE corporate R&D), "Kinetics of Oxidation of Carbide and Silicide Dispersed Phases in Oxide Matrices," *Advanced Ceramic Materials* **3** [5] 491-97 (1988).
28. J. Schlichting, "Molybdenum Disilicide as Component of Modern High Temperature Composites," *High Temp.- High Pressures*, **10** 241-69 (1978).
29. R. Brynsvold, "Processing of a Mullite Matrix, Molybdenum Disilicide Reinforce Composite," M.Sc. thesis, University of Washington (1991).
30. K. Niihara, "New Design Concepts of Structural Ceramics - Ceramic Nanocomposite," *J. Ceram. Soc. Jpn.*, **99** [10] 974-82 (1991).
31. H. Takada, A Nakahira, H. Ohnishi, S. Ueda, and K. Niihara, "Improvement of Mechanical Properties of Natural Mullite/SiC Nanocomposite," *Jpn. J. Powder and Powder Met.*, **38** 348-51 (1991).
32. S. Wu and N. Clausen, "Reaction Bonding and Mechanical Properties of Mullite/Silicon Carbide Composites," *J. Am. Ceram. Soc.* **77** [11] 2898-904 (1994).
33. N. Shinohara, unpublished research, University of Washington (1986).
34. N. Shinohara, D. M. Dabbs, and I. A. Aksay, "Infrared Transparent Mullite through Densification of Monolithic Gels at 1250°C," *Infrared and Optical Transmitting Materials*, R. W. Schwartz, ed., Proc. SPIE **683**, 12-18 (1986).
35. C. Han, G. D. Maupin, I. A. Aksay, G. C. Stangle, C. B. Martin, and R. P. Kurosky, "Ceramic Precursor Mixture and Technique for Converting the Same to Ceramic," U.S. Patent #5,061,682 (October 29, 1991).
36. G. L. Messing, S.-C. Zhang, and G. V. Jayanthi, "Ceramic Powder Synthesis by Spray Pyrolysis," *J. Am. Ceram. Soc.*, **76** [11] 2707-26 (1993).
37. Y. L. Zhang, D. L. Milius, I. A. Aksay, "Effect of Structural Morphology on the Mechanical Properties of SiC/A1 Ceramic-Metal Composites," *Proc. 5th International Symp. on Ceramic Materials and Components for Engines*, 1994.
38. T. Iseki, T. Kameda, and T. Maruyama, "Interfacial Reactions Between SiC and Al During Joining," *J. Mat. Sci.*, **19** 1692-1698 (1984).
39. T. Yano, S. Kato, and T. Iseki, "High Resolution Electron Microscopy of SiC/Al_4C_3 Interface,"
40. J. C. Viala, F. Bosselet, P. Fortier, and J. Bouix, "Chemical Aluminum or Aluminum-Silicon Alloys", *ICCM&ECCM,* **2** 2.147-2.155, F. L. Matthews, ed.
41. D. L. Milius, "The Sintering of Silicon Carbide with Liquid Aluminum," M.S. Thesis, University of Washington, 1986.
42. D. J. Lloyd and E. Dewing, "Stability of SiC in Molten Aluminum," D. S. Wilkinson, ed., 71-77 (Pergamon Press).
43. S. Schamm, J. P. Rocher, and R. Naslain, "Physicochemical Aspects of the K_2ZrF_6 Process Allowing the Spontaneous Infiltration of SiC (or C) Preforms by Liquid Aluminum," *Developments in the Science and Technology of Composite Materials, ECCM,* Vol. 3, 157-163 (1989).

44. M. Yasrebi, G. H. Kim, K. E. Gunnison, D. L. Milius, M. Sarikaya, and I. A. Aksay, "Biomimetic Processing of Ceramics and Ceramic- Metal Composites," *Mat. Res. Soc. Symp. Proc.*, **180** 625-635 (1990).
45. F. Delannay, L. Froyen, and A. Deruyttere, "Review: The Wetting of Solids by Molten Metals and it's Relation to the Preparation of Metal-Matrix Composites," *J. Matl. Sci.*, **22** 1-16 (1987).
46. S. Y. Oh, J. A. Cornie, and K. C. Russell, "Wetting of Ceramic Particles with Liquid Aluminum Alloys," *Met. Trans. A*, **20A** 527-41 (1989).
47. N. D. Corbin, G. A. Rossi, and P. M. Stephan, "Making Ceramics Tougher," *Machine Design*, 84-89 (July 23, 1987).
48. R. P. Andres, R. S. Averback, W. L. Brown, W. A. Goddard III, A. Kaldor, S. G. Louie, M. Moscovits, P. S. Peercy, S. J. Riley, R. W. Siegel, F. Spaepen, and Y. Wang, "Research Opportunities on Cluster And Cluster-Assembled Materials," *J. Mater. Res.*, **4** [3] 705-36 (1989).
49. R. W. Siegel, R. Ramasamy, H. Hahn, L. Tiang, and R. Gronsky, "Synthesis, Characterization, and Properties of Nanophase TiO_2," *J. Mater. Res.*, **3** 1367-72 (1988).
50. E. Ustundag, R. Subramanian, R. Dieckmann, and S. L. Sass, *In-Situ Composites: Science and Technology*, M. Singh and D. Lewis eds., p97 (The Minerals, Metals, and Materials Society, 1994).
51. E. Breval, Z. Deng, S. Chiou, and C. G. Pantano, *J. Mat. Sci.* **27** 1464 (1992).
52. R. Subramanian, E. Ustundag, R. Dieckmann, and S. L. Sass, in *Advances in Ceramic-Matrix Composites*, Edited by 127.
53. R. Roy, S. Komarneni, and D. M. Roy, in *Better Ceramics Through Chemistry*, Edited by C. J. Brinker, D. E. Clark, and D. R. Ulrich, *Mater. Soc. Symp. Proc.* **32** 347 (1984).
54. A. E. Nielsen, "Precipitates: Formation, Coprecipitation and Aging," in *Treatise of Analytical Chemistry, Part I, Theory and Practice*; 2nd ed., Vol. 5, I. M. Kolthoff and P. J. Elving, eds., 269-347 (Wiley, New York, 1983).
55. W. Hertl, "Kinetics of Barium Titanate Synthesis," *J. Am. Ceram. Soc.*, **71** [10] 879-83 (1988).
56. G. H. Bogush and C. F. Zukoski, "Studies on the Formation of Monodisperse Silica Powders", in *Ultrastructure Processing of Advanced Ceramics*, J. D. Mackenzie and D. R. Ulrich, eds., 477-486 (Wiley, New York, 1988).
57. Ishikawa et al., *Phys. Rev. B*, **37** 5852 (1988).
58. Uchino et al., *J. Am. Ceram. Soc.*, **72** 1555 (1989).
59. G. Arlt, D. Hennings, and G. de With, *J. Appl. Phys.* **58** 1619 (1985).
60. W. Y. Shih, W.-H. Shih, and I. A. Aksay, "Size Dependence of the Ferroelectric Transition of Small $BaTiO_3$ Particles: Effect of Depolarization," *Phys. Rev. B*, **50** [21] 15,575-85 (1994).
61. J. F. Scott and C. A. P. DeAraujo, "Ferroelectric Memories," *Science*, **246** 1400-05 (1989).
62. B. A. Tuttle, T. J. Headley, B. C. Bunker, R. W. Schwartz, T. J. Zender, C. L. Hernandez, D. C. Goodnow, R. J. Tissot, and J. Michael, "Microstructural Evolution of $Pb(Zr,Ti)O_3$ Thin Films Prepared by Hybrid Metallo-Organic Decomposition," *J. Mater. Res.*, **7** [7] 1876-82 (1992).

63. R. W. Schwartz, Z. Xu, D. A. Payne, T. A. DeTemple, and M. A. Bradley, "Preparation and Characterization of Sol-Gel Derived $PbTiO_3$ Thin Layers on GaAs," *Mat. Res. Soc. Symp.*, **200** 167-72 (1990).
64. K. D. Budd, "Structure Evolution in Sol-Gel Derived Lead Titanate-Based Materials, and Applications to the Processing of Thin Dielectric Layers," Ph.D. Thesis, University of Illinois (1986).
65. G. L. Messing, M. Kumagai, R. A. Shelleman, and J. L. McArdle, "Seeded Transformations for Microstructural Control in Ceramics," *Science of Ceramic Chemical Processing*, L. L. Hench and D. R. Ulrich eds., pp. 259-271 (John Wiley & Sons, New York 1986).
66. P. Bendale, S. Venigalla, J. R. Ambrose, E. D. Verink, and J. H. Adair, "Preparation of Barium Titanate Films at 55°C by an Electrochemical Method," *J. Am. Ceram. Soc.* **76** 2619-27 (1993).
67. K. Oseeo-Asare, F. J. Arriagade, and J. H. Adair, "Solubility Relationship in the Coprecipitation Synthesis of Barium Titanate: Heterogeneous Equilibria in the Ba-Ti-C_2O_4-H_2O-System," *Ceramic Powder Science II*, edited by: G. L. Messing, E. R. Fuller Jr., and H. Hausner, The American Ceramic Society Inc., Westerville, OH (1988).
68. M. M. Lencka and R. E. Riman, "Thermodynamic Modeling of Hydrothermal Synthesis of Ceramic Powders," *Chem. Mater.* **5** 61-70 (1993).
69. M. Yoshimura, S. E. Yoo, M. Hayashi, and N. Ishizawa, "Preparation of $BaTiO_3$ Thin Film by Hydrothermal Electrochemical Method," *Jap. J. Appl. Phys.* **28** 2007-2009 (1989).
70. J. Liu, W. Y. Shih, W.-H. Shih, M. Sarikaya, I. A. Aksay, "On the Growth and Monodispersity of Colloidal Gold Particles," to be submitted to *Langmuir* (1995).
71. J. Liu, "Structures and Properties of Colloidal Systems of Nanometer-Sized Particles," Ph.D. Dissertation, University of Washington (1990).
72. J. Turkevich, P. C. Stevenson, and J. Hillier, "A Study of the Nucleation and Growth Processes in the Synthesis of Colloidal Gold," *Trans. Faraday Soc., Disc.* **11** 55-75 (1961).
73. D. M. Dabbs, N. Yao, and I. A. Aksay, "Surfactant Mediated Deformation of Gold Particles," *Proc. Ann. MSA*, **52** 446-7 (1994).
74. G. S. Ferguson, M. K. Chaudhury, G. B. Sigal, and G. M. Whitesides, "Contact Adhesion of Thin Gold Films on Elastomeric Supports: Cold Welding Under Ambient Conditions," *Science*, **253** 776-8 (1991).
75. W. Y. Shih, W.-H. Shih, and I. A. Aksay, "Elimination of an Isolated Pore: Effect of Grain Size," *J. Mat. Res.* **8** [4] 1 (1995).
76. C. T. Kresge, M. E. Leonowicz, W. J. Roth, J. C. Vartuli, and J. S. Beck, "Ordered mesoporous molecular sieves synthesized by a liquid-crystal template mechanism," *Nature* **359** 710 (1992).
77. J. S. Beck, J. C. Vartuli, W. J. Roth, M. E. Leonowicz, C. T. Kresge, K. D. Schmitt, C. T.-W. Chu, D. H. Olson, E. W. Sheppard, S. B. McCullen, J. B. Higgins, and J. L. Schlenker, "A new family of mesoporous molecular sieves prepared with liquid crystal templates," *J. Am. Chem. Soc.* **114** 10834 (1992).
78. J. R. Milch, *J. Appl. Cryst.* **16** 198 (1983).
79. S. M. Gruner, J. R. Milch, and G. T. Reynolds, *Rev. Sci. Instrum.* **53** 1770 (1982).
80. M. D. McGehee, "Self-Assembling Mesoscopic Surfactant/Silicate Materials" Senior Thesis, Princeton University (1994).

81. Q. Huo, D. I. Margolese, U. Ciesla, P. Feng, T. E. Gier, P. Sieger, R. Leon, P. M. Petroff, F. Schuth, and G. D. Stucky, "Generalized synthesis of periodic surfactant/inorganic composite materials," *Nature* **368** 317 (1994).
82. P. T. Tanev, M. Chibwe, and T. J. Pinnavala, "Titanium-containing mesoporous molecular sieves for catalytic oxidation of aromatic compounds," *Nature* **368** 321 (1994).
83. B. C. Bunker, P. C. Rieke, B. J. Tarasevich, A. A. Campbell, G. E. Fryxell, G. L. Graff, L. Song, J. Liu, J. W. Virden, and G. L. McVay, "Ceramic thin-film formation on functionalized interfaces through biomimetic processing," *Science* **264** 48 (1994).
84. A. J. Panshin and C. de Zeeuw, *Textbook of Wood Technology*, (New York, McGraw-Hill 1980) p. 85.
85. P. Buurman, "Mineralization of Fossil Wood," *Scripta Geol.* **12** 1-42 (1972).
86. P. B. Kaufman, J. D. LaCroix, P. Dayanandan, L. F. Allard, J. J. Rosen, and W. C. Bigelow, "Silicification of Developing Internodes in the Perennial Scouring Rush (*Equisetum* hyemale var. affine) *Dev. Biol.* **31** 124-35 (1973).
87. D. M. Dabbs, D. R. Treadwell, W. C. Hicks, I. A. Aksay, and F. Kayihan, "Ceramic/Wood Composites," unpublished research (1992).
88. S. E. Keckler, "Incorporation of Silica into Wood Cell Walls," Senior Thesis, Princeton University (1994).

4. Personnel

Senior Research Personnel:

Ilhan A. Aksay	David L. Milius
Helen Chan	Mao-Xu Qian
Daniel M. Dabbs	Wan Y. Shih
Fatih Dogan	Matt Trau
Itaru Honma	Nan Yao

Graduate Research Personnel:

Donald B. Bidinger	Kirk M. Slenes
Chang-Min Chun	James Vartuli
W. David Clifton	

Undergraduate Research Personnel:

Sara E. Keckler	Dilshad Shahid
John S. Lettow	Uthara Srinivasan
Michael D. McGehee	Joe Teltser
John Mellowes	

Collaborators:

Shyamsunder Erramilli (Physics, Princeton University)

Sol M. Gruner (Physics, Princeton University)

Bernard Keimer (Physics, Princeton University)

Alexandra Navrotsky (Geophysics, Princeton Univ.)

Dudley A. Saville (Chemical Engr., Princeton Univ.)

Wei-Heng Shih (Materials Engineering, Drexel University)

5. Manuscripts

5.1. Published Journal Articles

RJ = Refereed Journal

1. (RJ40) L. Bergstrom, C. H. Schilling, and I. A. Aksay, "Consolidation Behavior of Flocculated Alumina Suspensions," *J. Am. Ceram. Soc.*, **75** [12] 3305-14 (1992).
2. (RJ46) J. S. Abel, G. J. Stangle, C. H. Schilling, and I. A. Aksay, "Sedimentation in Flocculating Colloidal Suspensions," *J. Mater. Res.*, **9** [2] 451-61 (1994).
3. (RJ47) Y.-N. Jun, D. M. Dabbs, I. A. Aksay, and S. Erramilli, "Processing of Monolithic Magnetic Gels for Magnetophoresis," *Langmuir* **10** [10] 3377-79 (1994).
4. (RJ50) Y. Sakka and I. A. Aksay, "Processing of Nanocomposites of Silicon Nitride-Mullite-Alumina by Reaction Sintering," *Nanostructured Materials*, **4** [2] 169-82 (1994).
5. (RJ51) W.-H. Shih, W. Y. Shih, S.-I. Kim, and I. A. Aksay, "Equilibrium-State Density Profiles of Centrifuged Cakes," *J. Am Ceram. Soc.*, **77** [2] 540-6 (1994).
6. (RJ52) W. Y. Shih, W.-H. Shih, and I. A. Aksay, "Elimination of an Isolated Pore: Effect of Grain Size," *J. Mater. Res.*, **9** (1994), submitted.
7. (RJ53) Y.-B. Son, C.-H. Kim, S.-D. Jang, J. Liu, M. Sarikaya, and I. A. Aksay, "Crystallization Behavior of Cordierite-Based Glass with Excess SiO_2 and Al_2O_3 at Initial Stage," *Jpn. J. Appl. Phys.*, **32**, Pt. 1, (1993).
8. (RJ54) Y. L. Zhang, D. L. Milius, I. A. Aksay, "The Effect of Si on the Wetting Behavior of SiC-A1 System," *Materials Science and Engineering* (Chinese), **12** [2] 16-23 (1994).
9. (RJ55) Y. Sakka, D. D. Bidinger, and I. A. Aksay, "Processing of SiC-Mullite-Al_2O_3 Nanocomposites," *J. Am. Ceram. Soc.*, **78** (1995).
10. (RJ56) W. Y. Shih, W.-H. Shih, and I. A. Aksay, "Elimination of an Isolated Pore: Effect of Grain Size," *J. Mater. Res.*, **10** [4] (1995).
11. (RJ57) M. Trau, S. Sankaran, D. A. Saville, and I. A. Aksay, "Field-induced Pattern Formation in Colloidal Dispersions," *Nature*, **373** (1995).
12. (RJ63) M. Trau, S. Sankaran, D. A. Saville, and I. A. Aksay, "Pattern Formation in Non-Aqueous Colloidal Dispersions via Electrohydrodynamic Flow," *Langmuir*, **11** 4665-72 (1995).
13. (RJ69) W. Y. Shih, W.-H. Shih, and I. A. Aksay, "Heteroflocculation in Binary Colloidal Suspensions: Monte Carlo Simulations," *J. Am. Ceram. Soc.*, (1996) (in press).
14. (RJ71) M Trau, D. A. Saville, and I. A. Aksay, "Field Induced Layering of Colloidal Crystals," *Science*, **272** [5262] (1996).
15. (RJ72) D. R. Treadwell, D. M. Dabbs, and I. A. Aksay, "Mullite ($3Al_2O_3 \cdot 2SiO_2$) Synthesis with Aluminosiloxanes," *Chem. Mater.*, (1996) (submitted).

5.2. Chapters in Books and Proceedings

IRP = Invited/Refereed Proceedings; IP= Invited Proceedings; and RP = Refereed Proceedings

1. (RP41) L. Bergstrom, C. H. Schilling, and I. A. Aksay, "Compressive Yield Stresses of Flocculated Particle Suspensions," in *Theoretical and Applied Rheology*, edited by P. Moldenaers and R. Keunings, Proc. XIth Int. Congr. on Rheology, Elsevier, Amsterdam, 1992, pp. 579-81.
2. (IRP12) L. A. Chick, C. Viney, and I. A. Aksay, "Phase Separation and Clustering in Systems of Rodlike Particles," in *Ultrastructure Processing of Advanced Materials*, edited by D. R. Uhlmann and D. R. Ulrich, (Wiley Interscience, New York, 1992), pp. 201-09.

3. (RP42) F. Dogan, J. Liu, M. Sarikaya, and I. A. Aksay, "A Study on the Formation of Hydrothermally Prepared $BaTiO_3$ Particles," in *Proc. 50th Ann. Meeting EMSA,* edited by G. W. Bailey (San Francisco Press, San Francisco, 1992), pp. 304-05.
4. (RP44) G. H. Kim, M. Sarikaya, and I. A. Aksay, "Measurement of Residual Stresses in B_4C-Al Cermets by CBED," in *Proc. 50th Ann. Meeting EMSA,* edited by G. W. Bailey (San Francisco Press, San Francisco, 1992), pp. 154-55.
5. (RP48) M. Sarikaya and I. A. Aksay, "Imaging of Hierarchically Structured Materials," in *Hierarchically Structured Materials, MRS Symp. Proc.*, Vol. 255, edited by I. A. Aksay, E. Baer, M. Sarikaya, and D. A. Tirrell, (Materials Research Society, Pittsburgh, Pennsylvania, 1992), pp. 293-307.
6. (CP49) H. Erkalfa, Z. Misirli, T. Baykara, F. Dogan, and I. A. Aksay, "Mechanical Properties of Colloidally Processed Alumina with Cr_2O_3 and MnO_2 Additives," in *Proc. of the Third Euro-Ceramics, Vol. 3*, edited by P. Duran and J. F. Fernandez (Faenza Editrice Ibérica, San Vicente, Spain, 1993), pp. 549-53.
7. (RP49) Y. Sakka, D. D. Bidinger, J. Liu, M. Sarikaya, and I. A. Aksay, "Processing of SiC-Mullite-Al_2O_3 Nanocomposite," in *Proc. 16th Annual Conf. Metal Matrix, Carbon, and Ceramic Matrix Composites*, edited by J. D. Buckley, NASA CP-3175 Part 1, (NASA Langley, February 1993), pp. 15-26.
8. (CP20) S. Sevinctav, T. Baykara, F. Dogan, and I. A. Aksay, "Monolithic α-Alumina Through Pressure Filtration of Seeded Boehmite Gels," in *Proc. of the Third Euro-Ceramics, Vol. 1*, edited by P. Duran and J. F. Fernandez (Faenza Editrice Ibérica, San Vicente, Spain, 1993), pp. 687-90.
9. (RP52) W.-H. Shih, W. Y. Shih, S.-I. Kim, and I. A. Aksay, "Equilibrium-State Density Profiles of Centrifuged Cakes of Flocculated Suspensions," *MRS Symp. Proc.*, **289**, 251-56 (Materials Research Society, 1993).
10. (RP53) D. M. Dabbs, N. Yao, and I. A. Aksay, "Surfactant Mediated Deformation of Gold Particles," in *Proc. 52nd Ann. Mtg. MSA,* eds.: G. W. Bailey and A. J. Garratt-Reed, (Microscopy Society of America, 1994), pp. 446-7.
11. (RP56) M. D. McGehee, S. M. Gruner, N. Yao, C. M. Chun, A. Navrotsky, and I. A. Aksay, "Synthesis of Mesoscopic Structures by Co-Assembly," *Proc. 52nd Ann. Mtg. MSA* (Microscopy Society of America, 1994).
12. (RP59) Y. L. Zhang, D. L. Milius, I. A. Aksay, "Effect of Structural Morphology on the Mechanical Properties of SiC/Al Ceramic-Metal Composites," *Proc. 5th International Symp. on Ceramic Materials and Components for Engines*, 1994.
13. (RP65) N. Yao, W. Y. Shih, D. M. Dabbs, and I. A. Aksay, "The Breakup of the Intermediate Gold Aggregates," in *Proc. Microscopy and Microanalysis,* eds.: G. W. Bailey, M. H. Ellisman, R. A. Hennigar, and N. J. Zaluzec, (Jones and Begell Pub., New York, 1995) pp. 196-97.
14. (RP66) C. M. Chun, A. Navrotsky, and I. A. Aksay, "Nucleation and Growth of $SrTiO_3$ on Nanometer-Sized $BaTiO_3$ Particles," in *Proc. Microscopy and Microanalysis,* eds.: G. W. Bailey (Jones and Begell Pub., New York, 1996) pp.
15. (RP67) C. M. Chun, A. Navrotsky, and I. A. Aksay, "Morphological Evolution of Nanometer-Sized $BaTiO_3$ Particles," in *Proc. Microscopy and Microanalysis,* eds.: G. W. Bailey (Jones and Begell Pub., New York, 1996) pp.

16. (RP68) N. Durlu, N. Yao, D. L. Milius, and I. A. Aksay, "Liquid Phase Sintering of BN Doped Fe-Cu/TiC Composites," in *Proc. Microscopy and Microanalysis,* eds.: G. W. Bailey (Jones and Begell Pub., New York, 1996) pp.
17. (RP69) N. Yao, D. M. Dabbs, and I. A. Aksay, "Mullite Phase Separation in Nanocomposite Powders," in *Proc. Microscopy and Microanalysis,* eds.: G. W. Bailey (Jones and Begell Pub., New York, 1996) pp.

5.3. Patents and Invention Disclosures

1. "Low Temperature Sintering of Ceramic Materials," M. Hama, D. M. Dabbs, and I. A. Aksay, U.S. Patent #5,135,691; August 4, 1992.
2. "Laminated B_4C/Al Composites through Melt Infiltration," I. A. Aksay, M. Yasrebi, D.L. Milius, G.-H. Kim, and M. Sarikaya, U.S. Patent #5,308,422, 1994.
3. "Method for Stabilizing Ceramic Suspensions," M. Yasrebi, H. Nakagawa, and I. A. Aksay, 1993.

6. Biographical Sketches

6.1. Ilhan A. Aksay

Dr. Aksay is a Professor in the Chemical Engineering Department and the Princeton Materials Institute at Princeton University. Prior to joining Princeton University, Dr. Aksay was a professor in the Department of Materials Science and Engineering at the University of Washington from 1983 through August 1992. He earned his B.Sc. degree (with honors) in Ceramic Engineering at the University of Washington in 1967. He received his M.Sc. degree in 1969 and Ph.D. in 1973, both in Materials Science and Engineering at the University of California, Berkeley. Upon completing a one-year postdoctoral appointment at the University of California, Berkeley, he worked at Xerox, Webster Research Center (1973-75) and the Middle East Technical University in Ankara (1975-81). In 1981, Dr. Aksay joined UCLA's Materials Science and Engineering Department as a visiting Associate Professor. In September 1983, he joined the faculty of the University of Washington as an Associate Professor in the Department of Materials Science and Engineering and was promoted to Professor in 1985. His most recent research activities have been on the utilization of colloidal and biomimetic techniques in ceramic processing. In recognition of his contributions in this area, he received the Richard M. Fulrath Award of the American Ceramic Society in 1987. In 1987, he was also named as the first Pacific Northwest Laboratory Professor by the U.S. Department of Energy. More recently, he received the Puget Sound Engineering Council's 1988 Academic Engineer of the Year award for his "contributions to advances in ceramic processing technology and the transfer of this technology to industry and students." Dr. Aksay is a Fellow of the American Ceramic Society.

Research Interests

- processing science of ceramics
- thermodynamics and phase equilibria
- diffusion and structural studies in ionic systems
- interfacial reactions and capillary phenomena
- utilization of colloidal and biomimetic techniques in ceramic processing

6.2. Daniel M. Dabbs

Daniel M. Dabbs received his B.Sc. degree in Chemistry at Texas Tech University in 1977. Both his M.Sc. degree (Physical Chemistry, 1979) and Ph.D. (Materials Science and Engineering, 1984) were awarded by the University of Washington. Upon completion of his doctoral work, he went to work for Wacker Siltronic (Portland, Oregon) as a Materials Characterization Engineer. In March of 1986, Dr. Dabbs joined the research group of Dr. Ilhan A. Aksay at the University of Washington as a Postdoctoral Research Associate. A year later, he accepted the position of Acting Program Manager, Advanced Ceramics Materials Laboratory, within the Washington Technology Center and College of Engineering, University of Washington; he was promoted to Program Manager in August 1987. In September 1992 Dr. Dabbs joined Princeton University as a Research Staff Member in the Ceramic Materials Laboratory. His research interests include vibrational spectroscopic characterization of ceramics and precursors, phase transitions in ceramic precursors, fiber-matrix interaction studies, and electron transfer mechanisms. He has also performed several studies in the physical chemistry of trace elements in crystalline material. As a graduate Research Assistant, his studies on the

behavior of arsenic in fayalitic slags earned him a Fellowship in the Washington Minerals Resource and Research Institute.

Research Interests

- vibrational spectroscopic characterization of ceramics and precursors
- phase transitions in ceramic precursors
- fiber-matrix interaction studies
- electron transfer mechanisms
- physical chemistry of trace elements in crystalline material

6.3. David L. Milius

David L. Milius received his B.Sc. degree in Ceramic Engineering from Iowa State University in 1984. In 1986 he received his M.Sc. in Ceramic Engineering from the University of Washington, Seattle; his thesis was entitled "The Sintering of SiC with Liquid Aluminum." Following graduation he went to work for the Advanced Ceramic Materials Laboratory in the Washington Technology Center at the University of Washington. From 1986 to 1992 he participated in a joint project on the processing of ceramic-metal composites with both the Lawrence Livermore National Laboratory and the Los Alamos National Laboratory. These materials were tested as potential lightweight armor materials for the Air Force Office of Scientific Research. In 1992 he joined the Princeton University as a Research Technical Staff Member in the Ceramic Materials Laboratory, Princeton Materials Institute. His interests include ceramic-metal composites, superconducting single crystals, and ceramic-ceramic nanocomposites. He has also worked on the processing of ceramics for engine component applications.

Research Interests

- processing and fabrication of ceramic-metal composites
- high temperature ceramic superconductors
- nanocomposites

6.4. Wan Y. Shih

Wan Y. Shih received her B.S. in Physics from Tsing-Hua University, Hsin-Chu, Taiwan, ROC, in 1976 and her Ph.D. in Physics from the Ohio State University, Columbus in 1984. She worked as a Postdoctoral Research Associate in the Materials Research Laboratory at the Ohio State University from 1984-1985. She worked as a Research Scientist in the Department of Materials Science and Engineering and the Washington Technology Center at the University of Washington, Seattle, from 1985 to 1992. Since 1993, she has held two simultaneous appointments: as a Research Staff Member in the Chemical Engineering Department and the Princeton Materials Institute, Princeton University, Princeton, New Jersey, and as a Research Associate Professor in the Department of Materials Engineering, Drexel University, Philadelphia.

Research Interests

- materials theory
- superconductivity
- dielectrics and ferroelectrics
- smart materials,

- numerical simulations
- structure and rheological properties of colloidal suspensions
- sintering of nanometer-size particles